Department of Applied Physics

Chemically modified and nanostructured graphene

Mari Ijäs

Aalto University

Chemically modified and nanostructured graphene

Mari Ijäs

A doctoral dissertation completed for the degree of Doctor of Science (Technology) to be defended, with the permission of the Aalto University School of Science, at a public examination held at the lecture hall E (Otakaari 1, Espoo) of the school on 13 September 2013 at 12.

Aalto University
School of Science
Department of Applied Physics

Supervising professor
Aalto Distinguished Professor Risto Nieminen

Thesis advisor
Adjunct Professor Ari Harju

Preliminary examiners
Doctor Pekka Koskinen, University of Jyväskylä, Finland
Doctor Ari Seitsonen, University of Zürich, Switzerland

Opponent
Professor Riccardo Mazzarello, RWTH Aachen, Germany

NORDIC ECOLABEL

441   697
Printed matter

Abstract

After its experimental discovery in 2004, graphene has been the topic of intense research. Its extraordinary linear dispersion relation in the vicinity of the Fermi surface allows the study of relativistic quantum mechanics in a condensed-matter context. The gapless spectrum is beneficial in, for instance, optical applications as the optical absorption is nearly constant in the visible spectrum. In transistor applications, however, the absence of a gap leads to poor on-off ratios. Thus, inducing a gap is of interest for applications, and both quantum confinement as well as chemical modification can be used to achieve this goal.

In this thesis, the electronic properties of modified graphene systems are studied using density-functional theory and lattice models. Additionally, a novel lattice density-functional theory approach is introduced. The chemical modification of graphene using chlorine and hydrogen is addressed considering also its chemical environment, a silicon dioxide substrate and a gaseous atmosphere treated using ab initio thermodynamics. Electronic states in finite metal-deposited graphene nanostructures with gaps induced by quantum confinement are studied together with experimental measurements. Finally, the prospect of superconductivity in rhombohedral graphite is addressed by studying flat bands in rhombohedral graphene multilayers.

The results add to the understanding of the electronic properties of graphene in complex environments. We clarify the effect of the substrate in hydrogen adsorption on graphene and provide a suggestion to prepare graphene nanoribbons using chlorine to unzip carbon nanotubes. We aid in the interpretation of recent scanning tunneling microscopy experiments on metal-deposited finite graphene nanostructures, as well as provide reference data for the detection of end states in graphene ribbons.

Tiivistelmä

  Grafeeni, tasomainen hunajakennomaisesti järjestäytyneistä hiiliatomeista muodostuva rakenne, on lupaava materiaali muun muassa optisiin sovellutuksiin. Tämä johtuu grafeenin vyörakenteesta, joka fermipinnan läheisyydessä muodostuu lineaarisista toisensa risteävistä energiavöistä. Täten grafeenin varauksenkuljettajat muistuttavat tietyiltä ominaisuuksiltaan relativistisia hiukkasia, mikä on poikkeuksellista kiinteän aineen fysiikassa. Energia-aukko valenssi- ja johtavuusvöiden välillä on kuitenkin toivottava joissain sovellutuksissa, esimerkiksi se mahdollistaisi voimakkaamman signaalin grafeenitransistorin tilojen välillä. Energia-aukko voidaan saada aikaan sekä liittämällä grafeeniin muita kemiallisia ryhmiä, että grafeenirakenteen dimensioita pienentämällä.

  Tässä väitöskirjassa tutkitaan kemiallisesti muokattujen ja äärellisten grafeenirakenteiden ominaisuuksia käyttäen tiheysfunktionaaliteoriaa ja hilamalleja, sekä esitellään grafeenin kuvaamiseen soveltuva nämä menetelmät yhdistävä hilatiheysfunktionaaliteoriamalli. Grafeenin sähköisten ominaisuuksien muokkaamista vedyn ja kloorin avulla tutkitaan huomioiden grafeenin kemiallinen ympäristö: piidioksidipinta sekä kaasuatmosfääri. Metallipinnoille syntetisoitujen grafeenihiutaleiden energiatiloja mallinnetaan yhteistyössä kokeellisten ryhmien kanssa. Lisäksi tarkastellaan suprajohtavuutta rhombohedrisesti järjestäytyneissä grafeenin monikerrosrakenteissa.

  Tutkimustyössä selvitettiin substraatin merkitys vedyn kiinnittymisessä grafeenin pinnalle. Lisäksi ehdotettiin menetelmää, jolla grafeeninauhoja voitaisiin valmistaa käyttämällä klooria hiilinanoputkia avaavana reagenssina. Työssä myös selitettiin teoreettisesti grafeeninanorakenteiden pyyhkäisytunnelointimikroskopiamittauksia. Samalla ennustettiin tunnusmerkkejä, joilla grafeenin reunalla olevaa vedyn määrää voidaan mahdollisesti tunnistaa pyyhkäisytunnelointimikroskopiamittausdatan perusteella.

Preface

When I started this work in the summer of 2010, I had no idea how fulfilling the journey leading to the doctoral degree would be. Looking back, I am privileged to have had this opportunity.

Most importantly, I am indebted to the people I have worked with. My instructor Dr. Ari Harju deserves my first and foremost thanks for his support and help during my studies. Without you, this book would never have been finished. I am grateful to my supervisor Prof. Risto Nieminen for accepting me as a doctoral student, and thus enabling my graduate studies in the first place. Especially during the early stages of my doctoral work, Dr. Paula Havu was my second instructor. I thank all my collaborators. In addition to collaborating within our own research group, I am privileged to have collaborated with scientists outside it at Aalto University (Prof. Peter Liljeroth and his group, as well as Prof. Nikolai Kopnin and Dr. Tero Heikkilä from the Low Temperature Laboratory), at Utrecht University (Prof. Daniël Vanmaekelbergh and Ass. Prof. Ingmar Swart together with their groups), as well as at Nokia Research Center (Dr. Pirjo Pasanen). These collaborations not only turned out to be scientifically fruitful, but also taught me the invaluable lesson how to communicate and collaborate with scientists coming from different backgrounds.

The work has been performed in the Quantum Many-Body Physics (QMP) group in the Department of Applied Physics, and the group is also part of the Academy of Finland Center of Excellence in Computational Nanoscience (COMP). I thank the members of the QMP for providing a pleasant working environment (even though I, at times, had little to contribute to some of the lunch discussions on football and birdwatching). Mikko Ervasti deserves a special mention for brewing the after-lunch coffee, and raising my awareness on the importance of lowering the center of the cof-

fee grounds before switching on the coffee maker.

To my family and friends
For support, encouragement and, occasionally, even a shoulder to cry on

Thank you.

Espoo, August 15, 2013,

Mari Ijäs

Contents

Contents

iv

List of Publications

This thesis consists of an overview and of the following publications which are referred to in the text by their Roman numerals.

I M. Ijäs, A. Harju. Lattice density-functional theory on graphene. *Physical Review B*, **82**, 235111, 2010.

II P. Havu, M. Ijäs, A. Harju. Hydrogenated graphene on silicon dioxide surfaces. *Physical Review B*, **84**, 205423, 2011.

III M. Ijäs, P. Havu, A. Harju, P. Pasanen. Spin-asymmetric graphene nanoribbons in graphane on silicon dioxide. *Physical Review B*, **84**, 041403(R), 2011.

IV M. Ijäs, P. Havu, A. Harju. Fracturing graphene by chlorination: A theoretical viewpoint. *Physical Review B*, **85**, 035440, 2012.

V M. Ijäs, P. Havu, A. Harju. Interaction of chlorine with Stone-Wales defects in graphene and carbon nanotubes, and thermodynamical prospects of chlorine-induced nanotube unzipping. *Physical Review B*, **87**, 205430, 2013.

VI S. K. Hämäläinen, Z. Sun, M. P. Boneschanscher, A. Uppstu, M. Ijäs, A. Harju, D. Vanmaekelbergh, P. Liljeroth. Quantum-confined electronic states in atomically well-defined graphene nanostructures. *Physical Review Letters*, **107**, 236803, 2011.

VII J. van der Lit, M. P. Boneschanscher, D. Vanmaekelbergh, M. Ijäs, A. Uppstu, M. Ervasti, A. Harju, P. Liljeroth, I. Swart. Suppression of electron-vibron coupling in graphene nanoribbons contacted via a single atom. *Nature Communications*, **4**, 2023, 2013.

VIII M. Ijäs, A. Uppstu, M. Ervasti, P. Liljeroth, I. Swart, A. Harju. Electronic states in finite graphene nanoribbons: Effect of charging and defects (14 pages). Accepted for publication in *Physical Review B*, 2013.

IX N. Kopnin, M. Ijäs, A. Harju, T. Heikkilä. High-temperature surface superconductivity in rhombohedral graphite. *Physical Review B*, **87**, 140503, 2013.

Author's Contribution

Publication I: "Lattice density-functional theory on graphene"

The author adapted the lattice density-functional theory method to the graphene system, wrote the code implementing it, performed all calculations and wrote the manuscript.

Publication II: "Hydrogenated graphene on silicon dioxide surfaces"

The author performed the thermodynamical stability analysis, wrote approximately half of the manuscript, prepared all the figures, and participated in analyzing the data.

Publication III: "Spin-asymmetric graphene nanoribbons in graphane on silicon dioxide"

The author performed all the calculations on the nanoribbon systems, analyzed the results, and wrote the manuscript.

Publication IV: "Fracturing graphene by chlorination: A theoretical viewpoint"

The author suggested the research topic, performed all calculations in the absence of the substrate, analyzed the results, and wrote the manuscript.

Publication V: "Interaction of chlorine with Stone-Wales defects in graphene and carbon nanotubes, and thermodynamical prospects of chlorine-induced nanotube unzipping"

The author performed all the calculations with Stone-Wales defects as well as the thermodynamical stability analysis, half of the calculations of the chlorination of pristine carbon nanotubes, analyzed the results and wrote the manuscript.

Publication VI: "Quantum-confined electronic states in atomically well-defined graphene nanostructures"

The author extracted the atomic coordinates of the graphene flakes from STM images, generated the tight-binding Hamiltonians, performed the calculations on the small hexagonal flakes, and participated in discussions and interpretation of the results as well as the preparation of the manuscript.

Publication VII: "Suppression of electron-vibron coupling in graphene nanoribbons contacted via a single atom"

The author performed all DFT calculations, contributed to the interpretation of the results and the preparation of the manuscript, and wrote the parts of the Supplementary information regarding the calculations.

Publication VIII: "Electronic states in finite graphene nanoribbons: Effect of charging and defects (14 pages)"

The author performed all DFT calculations, interpreted the results and wrote the manuscript, apart from the section with the many-body theory results.

Publication IX: "High-temperature surface superconductivity in rhombohedral graphite"

The author performed the DFT calculations, fitted the tight-binding model, prepared Figure 1, and wrote the Supplementary Information.

1. Introduction

Graphite, the three-dimensional carbon allotrope with a layered structure, has been known for centuries, and is used for a wide scale of applications on the industrial level. Lower-dimensional materials based on the same hexagonal carbon network were, however, discovered only recently. Fullerenes, zero-dimensional spherical carbon cages, were first reported in 1985 [1]. Their discovery was followed in 1991 by that of carbon nanotubes, the quasi-one-dimensional, all-carbon cylinders [2]. In some sense, a graphene sheet consisting of hexagonally arranged carbon atoms can be thought to be the basic unit in all of these structures. Piling it into a stack forms graphite, and rolling it up yields carbon nanotubes and fullerene cages. Originally, graphene was studied only to simplify the description of graphite. The results for a single layer were only of theoretical interest but, consequently, many of its extraordinary properties, such as the linear dispersion of the electronic bands close to the Fermi level, were predicted as early as in 1947 [3]. The current surge in the research interest on this material began in 2004, as the Nobel price winners Prof. A. Geim and Prof. K. Novoselov were able to transfer few-layer graphene films for the first time, and demonstrate the high electron mobility of the material [4]. Epitaxial graphite thin films had, however, been studied already in the 1960s and 1970s [5, 6] but the experiments by Geim and Novoselov also started a search for practical applications.

The hexagonal lattice structure of graphene gives rise to the linear electronic dispersion at the corners of the Brillouin zone [7]. The lattice is bipartite, meaning that the sites belonging to one sublattices are nearest neighbors only to sites belonging to the other sublattice. Figure 1.1(a) illustrates the structure of a graphene sheet, showing the carbon atoms belonging to the two sublattices as black and gray spheres. The two carbon atoms in the graphene primitive cell, shown as the blue parallelogramm in Figure 1.1(a), are non-equivalent, and consequently there are also two non-equivalent K points at the corners of the Brillouin zone in the recip-
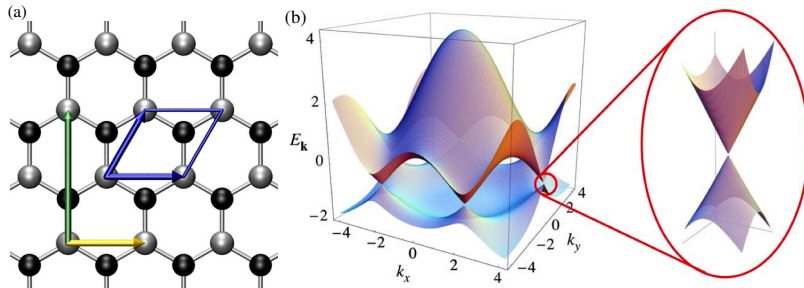
Figure 1.1. (a) The structure of the graphene lattice. The black and gray spheres denote the carbon atoms belonging to the A and B sublattices, respectively. The blue arrows show the primitive lattice vectors, and together with the blue lines they form the boundary of the two-carbon atom primitive unit cell. The yellow and green arrows show the zigzag and armchair directions, respectively, and they span an alternative rectangular four-carbon atom unit cell of the lattice. (b) The band structure of graphene in the reciprocal space. The K points with a linear electronic dispersion are located at the corners of the hexagonal Brillouin zone. Subfigure (b) is taken from Ref. [7].

rocal space. At these points close to the Fermi energy, the electronic bands of graphene form a cone, shown in Figure 1.1(b). For undoped graphene, the intersection points coincide with the points forming the Fermi surface. Because the low-energy dispersion is linear close to the intersection points, the electrons in graphene resemble massless particles [7]. In a way, graphene can be thought to be a condensed-matter testbed for relativistic quantum mechanics.

If the hexagonal lattice is confined into finite structures, two main edge directions are possible. These directions are called "armchair" and "zigzag" and they are illustrated in Figure 1.1(a) using green and yellow arrows, respectively. Obviously, other chiral edges interpolating between these extrema are possible, but a general edge is composed of finite armchair and zigzag segments. In finite graphene nanostructures, the electronic structure is sensitive both to the size of the graphene flake, as well as the edge termination. Long, planar stripes of graphene are called graphene nanoribbons (GNRs). The electronic structure of the ribbons depends on their edge termination. Zigzag-edged ribbons are predicted to be metallic and to have edge states with a flat dispersion [8]. The exchange interaction between electrons causes these states to be antiferromagnetically coupled across the ribbon, and also opens a band gap between them [7–9]. Armchair ribbons, on the other hand, can be either metallic or semiconducting depending on the ribbon width [7]. Experimentally, all ribbons prepared using lithographic methods seem to be semiconducting [10].

Graphene quantum dots, zero-dimensional graphene nanostructures, can also be thought of as aromatic macromolecules that have a discrete energy

spectrum. Similar to GNRs, their edge termination has a major impact on their electronic and optical properties. Similar to zigzag-edged GNRs, spin-polarized edge states are formed at the zigzag edges. In addition to zigzag GNRs, magnetic states in all-carbon structures have been predicted for triangular, zigzag-terminated graphene flakes [11].

A large number of potential applications have been suggested for graphene. The fact that graphene is a transparent conductor is probably its most important property, as such materials are needed, for instance, in solar cells. Here, just a few of the suggested applications are mentioned as illustrative examples. Zigzag-edged graphene flakes with spin-polarized edges have been proposed to act as spin logic gates [12]. Integrated graphene transistor structures with carbon-based electrodes and interconnects have been demonstrated [13], and the preparation of graphene field effect transistors is becoming a standard procedure [14]. In addition to electrical applications, devices based on the optical properties of graphene have been demonstrated [15], for instance mode-locked lasers [16] and photodetectors [17]. Other maybe less exciting uses for graphene include the use of graphene as a gas sensor [18] and as a filter in water desalination [19].

The original experimental fabrication method, mechanical exfoliation, yields irregular-shaped flakes, often with multilayered regions [4]. Recently, new methods for graphene synthesis have been introduced, and the originally far-fetched theoretical suggestions relying on precise control of the atomic structure of the graphene region are becoming experimentally feasible. In chemical vapor deposition, carbon-containing precursor such as methane is deposited on a transition metal surface and at elevated temperatures, polycrystalline sheets of monolayer graphene even in the size of a liquid crystal display screen can be synthesized [20]. The growth can be restricted to submonolayer coverage by controlling the amount of the precursor, temperature, the reaction time, and other experimental parameters. Moreover, the shape of the resulting graphene flakes can be somewhat controlled using post-annealing [21]. Finite graphene regions can be also formed by etching but in this approach, the edges are typically rough [22]. Very recently, a synthesis method for well-defined graphene nanostructures has been demonstrated using the polymerization of aromatic molecules on a catalytic surface [23]. Armchair-edged GNRs [23] and triangles [24], and even nanoribbon junctions composed of chevron-shaped ribbons [23] have been reported. The advantage of the method is that the structure precursor molecule determines the edge termination of the resulting nanostructure. Conversely, engineering a graphene nanostructure with a given shape requires complex precursor molecules

and, at the moment, precursors yielding a clean, zigzag-terminated edge are not known. Other graphene preparation methods include thermal annealing of SiC surfaces [25] and unzipping of carbon nanotubes [26]. For the preparation of high-quality monocrystalline graphene flakes with few defects, mechanical exfoliation still seems to be the method of choice.

In some applications, such as transistors, a band gap would be desirable instead of the linear gapless dispersion. In addition to lateral confinement, also the substrate and functionalization can be used to modify the properties of graphene. The choice of a substrate has an effect on doping, structural corrugation, and the screening of electron-electron interactions. For example, in suspended graphene samples, the Fermi velocity has been found to increase to over twofold [27] compared with the usually reported value of 10^6 m/s [7]. On the other hand, on silicon wafers covered by thermal silicon dioxide, the roughness and variation in the surface composition lead to the formation of charge puddles, variations in local potential [28], whereas on atomically smooth boron nitride, graphene properties differ a little from those in suspended samples [29]. In functionalizing graphene, attaching other chemical species directly to the carbon backbone may open a gap [30]. The functionalizing species either can be bound above the carbon plane, as is the case for hydrogen and fluorine [30–32], or it may substitute carbon atoms in the hexagonal network, like nitrogen [33] or boron [34]. In multilayer graphene, the interlayer interaction leads to a modified band dispersion at the corners of the Brillouin zone. For instance, in bilayer graphene the electronic dispersion is parabolic instead of linear at the K point [7] and an electric field can be used to open a band gap [35].

In this thesis, the electronic properties of chemically functionalized and laterally confined graphene systems are studied using density-functional theory and lattice models. Chapter 2 reviews the computational models used in Publication II-Publication IX, and also presents the novel lattice density-functional theory model introduced in Publication I. Chapter 3 highlights the main results for each of the studied graphene systems, and gives some background from the literature. Chapter 4 summarizes the publications included in this thesis.

2. Computational modeling of graphene

The full many-body problem of interacting electrons can be solved numerically exactly for only few-electron systems, such as small molecules, even if the electronic and atomic degrees of freedom are decoupled by applying the Born-Oppenheimer approximation. In addition to this, approximations simplifying either the numerical treatment of the full electron-electron interaction, or the interaction term itself are unavoidable.

Two main approaches are widely used. Some of the atomic orbitals can be neglected, including in the model only those accommodating the high-energy valence electrons close to the Fermi level. If these orbitals are assumed to be localized on the atomic sites, and the interaction between them is described with electrons hopping between orbitals localized on adjacent lattice sites, the model is said to be *tight-binding*. The Hamiltonian for such a model is thus determined by the energies and the overlaps of the orbitals, as well as the hopping amplitudes between them. The electron-electron Coulomb interaction is thus not explicitly included, and the electron density between the atomic sites is neglected. Electron-electron interactions can, however, be added on top of this kinetic model, for instance by introducing a Hubbard-type on-site repulsion between opposite-spin electrons occupying the same orbital [36]. Even if such models are simple, they have been found to describe graphene fairly well [7].

Alternatively, the full orbital structure of the atoms is taken into account but the Coulomb interaction is treated in an approximative manner. There are highly accurate quantum chemical approaches, such as the configuration interaction or the coupled-cluster methods that are capable of treating small molecules at high accuracy. This is not possible for larger molecules and periodic bulk structures, and a widely-used approximate solution is to use density-functional theory (DFT). The main idea of DFT is that the electron density, instead of the more complicated wavefunction is used as the basic variable, and all observables are calculated from it. The Coulomb interaction is treated on the Hartree-Fock mean-field level,
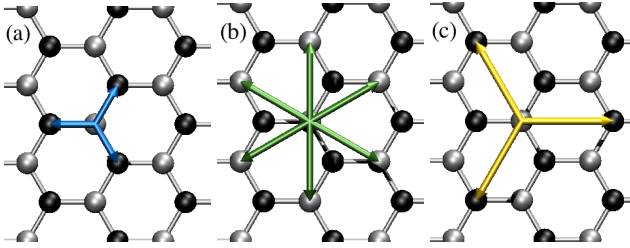
Figure 2.1. The atomic sites connected through (a) first-nearest neighbor (b) second-nearest neighbor (c) third-nearest neighbor hopping elements of the tight-binding model. The black and gray carbon atoms indicate the carbon atoms belonging to the A and B sublattices, respectively.

and correlation and exchange beyond it are treated using an exchange-correlation functional.

This Chapter introduces the models used to study graphene in this thesis, starting from the simpler lattice models, and then proceeding to a continuum description within the framework of density-functional theory. To bridge these two main approaches, a novel method developed in Publication I, lattice density-functional theory (LDFT) for graphene, is also described.

2.1 The tight-binding model

In the most widely-used tight-binding model for graphene, only the π electron system formed from the carbon p_z orbitals is used to describe the electronic properties close to the Fermi energy. In the case of finite graphene fragments, the dangling σ-type bonds at the edges are implicitly assumed to be terminated by hydrogen atoms. As the sp^2-hybridized σ orbitals composed of s, p_x and p_y carbon orbitals are much lower in energy, they can be excluded from the model [7]. Usually, the orbitals centered at different lattice sites i and j are assumed to be orthogonal, so that the orbital overlap between $|p_z^i\rangle$ and $|p_z^j\rangle$ is given by $\langle p_z^i|p_z^j\rangle = s_{ij} = \delta_{ij}$, but the overlap can also be explicitly included by using the overlap matrix S.

The hopping integrals between close-lying lattice sites describe an electron tunneling between a pair of p_z orbitals on sites i and j. They thus contain the kinetic contribution to the total energy due to electron movement on the lattice. A particular tight-binding parameterization is determined by the choice of these hopping amplitudes $\{t_{ij}\}$. For instance, the third-nearest neighbor (3NN) tight-binding model contains electron hoppings between atoms up to the third-nearest neighbor sites, as shown in Figure 2.1. The original tight-binding description of graphene [3] includes

only the nearest-neighbor (1NN) hopping t, which is often used as the unit of energy.

Once the set $\{t_{ij}\}$ is chosen, the tight-binding Hamiltonian is given by

$$H = \sum_{i,j} (t_{ij} c_i^\dagger c_j + t_{ij}^* c_j^\dagger c_i), \qquad (2.1)$$

where $c_i^{(\dagger)}$ is the electron annihilation (creation) operator in the second-quantized form. In periodic systems, a phase factor of the form $e^{i\vec{k}\cdot(\vec{r}_i - \vec{r}_j)}$ enters the hopping amplitude for sites connected over the periodic boundary. Here $\vec{k}$ is the wave vector in the reciprocal space, and $\vec{r}_i$ and $\vec{r}_j$ are the coordinates of the lattice sites. Structural imperfections or gating can be modeled using local potentials that change the orbital energies. A term describing the effect of the external potential on each of the lattice sites is added to the Hamiltonian, and it is of the form

$$V_{\text{ext}} = \sum_i \epsilon_i n_i, \qquad (2.2)$$

where ϵ_i is the strength of the potential on site i and $n_i = c_i^\dagger c_i$. The eigenvalue equation $H\Psi = E\Psi$ (or the generalized eigenvalue equation $H\Psi = ES\Psi$ if the overlap matrix $S_{ij} = s_{ij}$ is not unity) is then solved. The resulting one-electron states are occupied starting from the one lowest in energy up to the Fermi level.

The values of the hopping parameters $\{t_{ij}\}$ are, in general, fitting parameters determined by comparing, for instance, the band structure calculated using the tight-binding Hamiltonian with a reference such as a DFT calculation or experimental data, if available. Thus, in most cases the values cannot be thought to be exact, or to carry an explicit physical meaning. In the 1NN graphene tight-binding model, however, the value of the first nearest-neighbor hopping is related to Fermi velocity v_F, given by the slope of the linear dispersion at the corners of the Brillouin zone as $v_F = 3ta/2$, where $a \approx 2.46$ Å is the graphene lattice parameter [7]. The second-nearest neighbor in-plane parameter introduces trigonal warping and particle-hole asymmetry [7]. The earliest tight-binding parameterizations [3, 37] were fitted to the experimentally known properties of graphene, such as diamagnetic susceptibility. Further parameterizations to the transport properties of graphene nanoribbons [38], gated bilayer graphene [39], and even to double-resonance Raman spectroscopy of bilayer graphene [40] have been suggested.

Also multilayer graphene can be described within the tight-binding framework. Similar to bulk graphite, the adjacent layers are coupled through weak van der Waals-type interactions. There are two different stack-

(a)

(b)
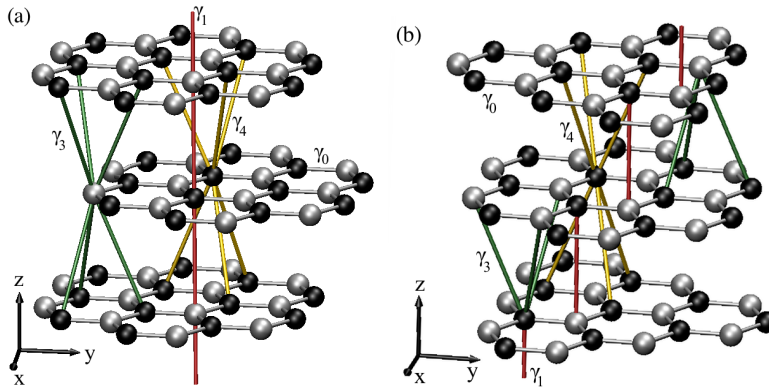
Figure 2.2. The structure of graphite or multilayer graphene with (a) the Bernal (b) rhombohedral stacking order, as well as the minimal hopping parameters used in the McClure [37] tight-binding model. Red lines show the vertical coupling between nearest-neighbor carbon planes (γ_1), green lines are nearest-neighbor out-of-plane couplings between sites belonging to the different sublattices (γ_3), and yellow lines out-of-plane couplings connecting sites belonging to the same sublattice (γ_4). In-plane bonds represent the nearest-neighbor hopping (γ_0).

ing sequences in multilayers with aligned primitive unit cells. Multilayer structures with misaligned unit cells in adjacent layers, also called twisted multilayers, are experimentally relevant [41, 42] but considering them is outside the scope of this thesis. Figure 2.2 illustrates the two stacking sequences, and the lattice sites that are connected by the tight-binding hopping amplitudes. In the Bernal stacking, the carbon atoms belonging to the A and B sublattices of the adjacent layers form a chain perpendicular to the plane of the hexagonal network, with A and B atoms being on top of each other in an alternating manner [Figure 2.2(a)]. In the rhombohedral stacking, each layer is displaced by one third of the primitive unit cell with respect to the one beneath it. The A-sublattice carbon atom is always on top of the B-sublattice carbon atom of the layer beneath [Figure 2.2(b)].

In addition to the in-plane tight-binding parameters, out-of-plane hoppings between the layers need to be included in the tight-binding Hamiltonian. In the model shown in Figure 2.2, only nearest-layer hoppings in the out-of-plane direction are included. The symbol γ has been used instead of t to denote the hopping parameter, in order to keep the notation for graphene multilayers similar to literature [7, 37]. γ_1 denotes the nearest-neighbor hopping amplitude between the carbon atoms located on top of each other, and γ_3 and γ_4 are the next-nearest neighbor hopping amplitudes between the layers. γ_3 and γ_4 connect carbon atoms belonging to a different and the same sublattice, respectively. Figure 2.2 also

clarifies how the two stacking sequences differ in terms of hopping amplitudes, most easily seen for the sites connected by green lines showing the γ_3 coupling. In the Bernal stacking, each carbon atom couples through γ_3 to both adjacent layers, whereas in the rhombohedral stacking, depending on the sublattice of the carbon atom, the coupling occurs either to the layer above or below. A few differing sets of included coupling have been used in the literature [7, 37, 43].

It is worth noting that, in general, the graphene tight-binding models contain some interaction effects on the mean-field level. This is due to the fitting procedure as the DFT band structures, to which the fits are usually made, contain the Coulomb interaction on a mean-field level. Thus, if the electron-electron interaction is to be explicitly included on top of the tight-binding model, this implicit mean-field component should first be removed [44].

2.2 The Hubbard model

Even though the tight-binding model can successfully be used to describe many graphene properties such as transport [38] and Landau levels in a magnetic field [7], the neglect of electron-electron interaction beyond the implicit mean-field level means that the magnetic properties cannot be described. The importance of the electron correlations in graphene is still being debated [7, 45]. If a tight-binding-based description is to be used to describe the magnetic properties of graphene, for instance the spin-polarized states localized at the zigzag-terminated edges [46], an interaction term including the electron exchange needs to be added to the tight-binding Hamiltonian.

In fact, considering only the on-site component of the Coulomb repulsion, the repulsion between electrons of opposite spin residing on the same lattice site, is enough to describe such magnetic properties. The Hubbard Hamiltonian for graphene thus consists of the kinetic contribution H_{kin}, given by the tight-binding Hamiltonian, Eq. (2.1), and the on-site interaction term H_U,

$$H_{\mathrm{Hub}} = H_{\mathrm{kin}} + H_U = \sum_{i,j,\sigma} t_{ij\sigma}(c_{i\sigma}^\dagger c_{j\sigma} + c_{j\sigma}^\dagger c_{i\sigma}) + \sum_i U_i n_{i\uparrow} n_{i\downarrow}. \qquad (2.3)$$

Here, $\sigma \in \{\uparrow, \downarrow\}$ is the spin index, U_i is the strength of the on-site interaction at site i, and $n_{i\sigma} = c_{i\sigma}^\dagger c_{i\sigma}$. Similar to the tight-binding model, a term describing the external potential [Eq. (2.2)] can be added to the Hamiltonian. In graphene, the kinetic term is spin-degenerate, $t_{ij\sigma} = t_{ij}$, but in

the general case, this is not required.

In the following, two different approaches to solve the model are considered. First, the exact diagonalization method applicable to small systems is described. Second, the mean-field approximation allowing one to solve larger systems is considered.

2.2.1 Exact diagonalization

As the name suggests, "exact diagonalization" refers to diagonalizing the Schrödinger equation $H|\Psi\rangle = E|\Psi\rangle$ in the full many-body basis. In a lattice model consisting of N lattice sites, the size of the full Hilbert space with $N_{\mathrm{el}} = N_\uparrow + N_\downarrow$ electrons is given by

$$N_{\mathrm{basis}} = \sum_{N_\uparrow} \binom{N}{N_\uparrow}\binom{N}{N_\downarrow}. \tag{2.4}$$

This is thus equivalent to the number of ways to distribute $N_\uparrow$ and $N_\downarrow$ indistinguishable particles onto N sites, and summing over all possible combinations of $N_\uparrow$ and $N_\downarrow$ under the constraint given by N_{el}.

The many-body basis is constructed from single-electron orbitals. There are two obvious choices for the single-electron basis: a localized basis, in which each of the lattice sites is either occupied or occupied by an electron, and the one-body basis, in which the eigenstates of the non-interacting model [H_{kin} in Eq. (2.3)] are used. Depending on the form of the interaction, the use of one of these choices might be favored in terms of the computational cost. For instance, in the lattice site basis, the on-site Hubbard interaction H_U contributes only to the diagonal of the full many-body Hamiltonian, whereas for a single-electron orbital basis, off-diagonal terms are present.

For a fixed number of electrons, $N_{\mathrm{el}} = N_\uparrow + N_\downarrow$, different values of $S_z = \frac{1}{2}|N_\uparrow - N_\downarrow|$ are possible. As there are no spin-flip processes in the Hubbard Hamiltonian, sectors with a different value of S_z do not couple, and the Hamiltonian can be diagonalized separately in each subspace. The size of the Hilbert space is thus greatly reduced. There are efficient numerical algorithms for solving the resulting sparse eigenvalue problem. The one used in Publication I is the Lanczos algorithm [47] that is based on the transformation of the Hamiltonian matrix to a tridiagonal form in the Krylov space. When the ground-state wavefunction is found, all observables such as site occupations or the total spin of the system can be calculated from it.

2.2.2 Hartree-Fock mean-field solution

The size of the full Hilbert space of the Hubbard model increases much faster than the number of lattice sites, and eventually obtaining the exact solution becomes first impractically slow, and then impossible due to computational limitations. The electron-electron interaction can, however, be treated in a mean-field manner. In the regime of relatively weak interaction, this approach captures the system behavior fairly well in terms of magnetic order, for instance, and compromises between accuracy and computational cost. Imposing the Hartree-Fock approximation, the ground-state of the interacting system is assumed to be expressible as a single Slater determinant constructed from the self-consistently optimized spin-orbitals. Each electron feels the average repulsion due to all other electrons. Exchange interaction between electrons is treated exactly, whereas electron correlations between opposite-spin electrons are neglected [48].

In the case of the Hubbard model, the electron-electron interaction is local [Eq. (2.3)]. On each site, the electrons only feel the repulsion caused by the opposite-spin electron density residing on the same site. The interaction part of the Hamiltonian becomes

$$H_U \approx \sum_{i\sigma} U_i n_{i\sigma} \langle n_{i-\sigma} \rangle, \tag{2.5}$$

where $\langle n_{i\sigma} \rangle$ denotes the density of spin σ electrons on site i. The full mean-field Hubbard Hamiltonian is given by

$$H_{MF,\sigma} = \sum_{ij} (t_{ij\sigma} c_{i\sigma}^\dagger c_{j\sigma} + t_{ij\sigma}^* c_{j\sigma}^\dagger c_{i\sigma}) + \sum_{i} (\epsilon_{i\sigma} + \langle n_{i-\sigma} \rangle) n_{i\sigma}, \tag{2.6}$$

where a term describing an external potential $\epsilon_{i\sigma}$ [Eq. (2.2)] has been included. Thus, electrons belonging to spin species σ are coupled to $-\sigma$-electrons by the effective on-site potential $\epsilon_i + \langle n_{i-\sigma} \rangle$, and the ground-state of the Hamiltonian has to be solved self-consistently. The Hartree-Fock spin orbitals are expanded in a one-body basis, for example the lattice sites of the underlying tight-binding model, and Eq. (2.6) is solved for both spin sectors. The N_σ lowest orbitals are occupied, the new effective potential is calculated, and the cycle is repeated until convergence in total energy or site occupations is achieved.

2.3 Density-functional theory

In many-body quantum theory, the wavefunction $|\Psi\rangle$ is the fundamental variable that contains all information on the state of the system, and

from which the expectation values of observables are calculated. For most interacting many-electron systems, the exact analytical solution for $|\Psi\rangle$ from the Schrödinger equation is not available and numerically exact solutions can be computed only for very small systems. The main idea of density-functional theory (DFT) is that the ground-state wavefunction $|\Psi(\vec{r})\rangle$, which depends on the $3N_{el}$ spatial coordinates, can be replaced by a much simpler object, the N_{el}-electron density $n(\vec{r})$ that is a function of only three spatial coordinates. This mapping was proved in 1964 by P. Hohenberg and W. Kohn [49]. The first Hohenberg-Kohn theorem states that for electrons moving in an external potential, such as the potential caused by the nuclei, the ground-state density is uniquely determined. This is a one-to-one correspondence, meaning that conversely, the potential is uniquely determined by the density. The second theorem relates the ground-state density to the ground-state energy by stating that there is a universal energy functional $E[n]$. Minimizing $E[n]$ with respect to n gives the exact ground-state density. As the ground-state density is directly obtained from the ground-state wavefunction, the ground-state density can be used to describe the system instead of the wavefunction.

The Hohenberg-Kohn theorems provide the theoretical justification for using the electron density instead of the wavefunction to describe the many-electron system. They do not, however, provide any concrete means to actually calculate this density. DFT became practical when Kohn and Sham [50] formulated a mapping between the fully interacting many-body system and an effective one-body problem in a modified external potential. This Kohn-Sham potential $v_{\mathrm{KS}}(\vec{r})$, is obtained through the constrained minimization of the energy functional $E[n]$ with respect to a variation in the one-electron orbitals $|\Psi_i\rangle$. The potential can be divided into terms resulting from the original external potential $v_{\mathrm{ext}}(\vec{r})$, the Hartree potential $v_{\mathrm{H}}(\vec{r})$ describing the electrostatic interaction between electrons, and a third term, $v_{\mathrm{xc}}(\vec{r})$, containing all the electron-electron interaction terms not included in the Hartree potential such as correlations. All in all, this gives the form

$$v_{KS}(\vec{r}) = v_{\mathrm{ext}}(\vec{r}) + v_{\mathrm{H}}(\vec{r}) + v_{\mathrm{xc}}(\vec{r}) \qquad (2.7)$$

for the Kohn-Sham potential. The ground-state density is then obtained by solving the one-electron Schrödinger equation

$$[\hat{T} + v_{\mathrm{KS}}]|\Psi_i\rangle = \epsilon_i|\Psi_i\rangle \qquad (2.8)$$

for the Kohn-Sham eigenstates and eigenenergies $|\Psi_i\rangle$ and ϵ_i, respectively,

and by constructing the ground-state density from the obtained orbitals,

$$n(\vec{r}) = \sum_{i}^{N_{\mathrm{el}}} |\langle \vec{r} | \Psi_i \rangle|^2 \,. \tag{2.9}$$

As $v_{\mathrm{KS}}(\vec{r})$ is a functional of $n(\vec{r})$, the problem has to be solved self-consistently, similar to the mean-field Hartree-Fock approximation to the Hubbard model.

Density-functional theory would be exact if the exact form for the exchange-correlation potential v_{xc} was known. Unfortunately, this is not the case and for all practical applications, this term has to be approximated. Frequently, the exchange-correlation term is composed into its exchange and correlation energy parts that are approximated separately, $E_{\mathrm{xc}} = E_{\mathrm{x}} + E_{\mathrm{c}}$. The exchange-correlation potential is the functional derivative of E_{xc} with respect to the density n, given by $v_{\mathrm{xc}} = \delta E_{\mathrm{xc}}/\delta n$.

In the simplest approximation to E_{xc} called the local density approximation (LDA), E_{xc} is assumed to depend only locally on the electron density, and this dependence is assumed to be that of homogeneous electron gas [48]. This approach can easily be extended to treat the densities of both spin species in spin-polarized systems. Allowing E_{xc} to depend also on the local gradients of the electron density leads to gradient-corrected functionals (GGAs), such as PBE [51] widely used in this thesis. A number of improved functionals have been developed, for instance hybrid functionals mixing a portion of the exact Hartree-Fock exchange to a LDA- or GGA-type functional, and meta-GGAs also depending on the kinetic energy density. An extensive review on the functionals that are available is not within the scope of this thesis, and the interested reader is referred to the literature, such as Ref. [52]. The all-electron FHI-aims code [53] using localized numeric atomic orbitals as the basis set was used in most DFT calculations in this thesis.

DFT is a ground-state theory. The Hohenberg-Kohn theorems only state that the exact ground-state energy can be obtained by minimizing the energy functional. No physical meaning can be, however, given to the individual Kohn-Sham eigenvalues. The only exception is the energy of the highest occupied Kohn-Sham state, the energy of which is related to the first ionization potential of the system [54]. The energy difference between the highest occupied and lowest unoccupied Kohn-Sham state is commonly used to approximate the band gap, and it is widely known that this approach underestimates the actual gap due to the absence of the derivative discontinuity in the exchange-correlation potential. The Hartree-Fock approach, on the other hand, overestimates this discontinuity, and thus hybrid functionals that mix a portion of Hartree exchange

yield larger band gaps than LDA or GGAs, partly correcting the underestimation. The GW approximation [55], based on a perturbative expansion in the DFT-based Green's function G and a screened long-range Coulomb interaction W, was developed to access the unoccupied side of the spectrum but it has been found also to improve the predictions on the magnitude of the band gap. In order to access to excited-state properties such as optical spectra, also time-dependent density-functional theory [56] and the solution to the Bethe-Salpeter equations [57], which includes excitonic contributions arising from the interaction between an excited electron and hole, are available.

2.4 Lattice density-functional theory

The main idea of DFT, which is that the interacting many-body system can be treated as a one-body problem in an effective potential so that the resulting ground state density corresponds to that of the many-body problem, can also be used for lattice Hamiltonians. In contrast to conventional continuum DFT, the density, the effective one-body potential and the Kohn-Sham Hamiltonian become discrete in the lattice formulation.

The idea of combining a lattice Hamiltonian and the approximations of DFT might seem counterintuitive at first. It can, however, be used for a number of purposes. An interacting lattice model, such as the Hubbard Hamiltonian, can be solved approximately using less computational effort, allowing one to increase the system size and treat correlations better than when using the plain Hartree-Fock approximation. On the other hand, such a simplified description can also be used as a testbed, in which the formal questions of DFT, such as the characteristics of the exact but unknown exchange-correlation functional and its discontinuities [58, 59] or the so-called v-representability problem [60, 61] can be studied.

Similar to continuum DFT, the electron-electron interaction effects apart from the Hartree potential are contained in the exchange-correlation functional. As the exact form is unknown, it has to be determined either numerically or from the analytical solution of a homogeneous reference system, if it is available. In the case of the Hubbard model, the analytical solution is available only in the one-dimensional case [62].

In Publication I, an exchange-correlation functional was parametrized for graphene, described by the Hubbard Hamiltonian on the honeycomb lattice, within the local density approximation. The exchange-correlation energy per lattice site, $e_{\mathrm{xc}}(n, U)$, was defined as the difference between the
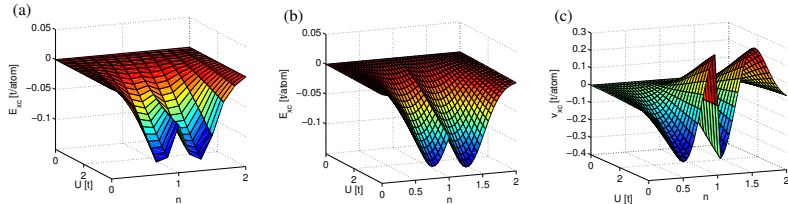
Figure 2.3. Parameterizing a LDFT exchange-correlation functional (a) The exchange-correlation energy surface, e_{xc}, calculated using a third-nearest neighbor hopping tight-binding as the kinetic part of the Hubbard model. (b) Eq. (2.11) fit to the data shown in subfigure a. (c) v_{xc} obtained from the fitted e_{xc} by numerical differentiation.

ground-state energy of the reference system calculated using exact diagonalization, $E(n, U)$, and its Hartree-Fock mean-field solution, $E_{\mathrm{HF}}(n, U)$, assuming that the electron density is homogeneous,

$$e_{\mathrm{xc}}(n, U) = \frac{E(n, U) - E_{\mathrm{HF}}(n, U)}{N}. \tag{2.10}$$

Here, n is the total electron density $n = (N_\uparrow + N_\downarrow)/N = \sum_i n_i$, where $i = 1...N$ runs over the lattice sites.

The reference system was chosen to be a periodic graphene supercell consisting of 2×6 sites. The Hubbard model was solved for all electron fillings $n = 0...2N_{\mathrm{el}}/N$, and the values of $S_z = (N_{\mathrm{el},\uparrow} - N_{\mathrm{el},\downarrow})/2$ in the range $U = [0, 4t]$. Figure 2.3(a) shows the e_{xc} surface determined using the third-nearest neighbor tight-binding model as the kinetic part of the Hamiltonian. The functional fit was, however, done to the case with the smallest spin polarization, $S_z = 0$ and $S_z = 1/2$, as due to the small number lattice sites, the amount of data was not sufficient for a good fit for higher values of S_z. A smooth function of the form

$$e_{\mathrm{xc}}(n, U) = \alpha_1 (e^{-\alpha_2 U^2} - 1) e^{-[\alpha_3(1-|n-1|)-\alpha_4]^2}, \tag{2.11}$$

where α_i are the fit parameters, was then fitted to the resulting exchange-correlation energy surface, shown in Figure 2.3(b). The exchange-correlation potential v_{xc} was then obtained by numerically deriving the fit, Figure 2.3(c), as

$$v_{\mathrm{xc}}(n, U) = \frac{\partial e_{\mathrm{xc}}(n, U)}{\partial n}. \tag{2.12}$$

To find out whether the exchange-correlation potential was transferable to non-periodic graphene systems, the resulting LDFT model with e_{xc} given by Eq. (2.10) was compared to the exact solution of the Hubbard model in the case of a 16-atom finite graphene flake, shown in Figure 2.4(a). At quarter-filling without impurities, the ground-state energies were found to improve over their mean-field Hartree-Fock counterparts to within 1% of their exact values [Figure 2.4(b)]. Even at half-

(a)

(b)

(c)
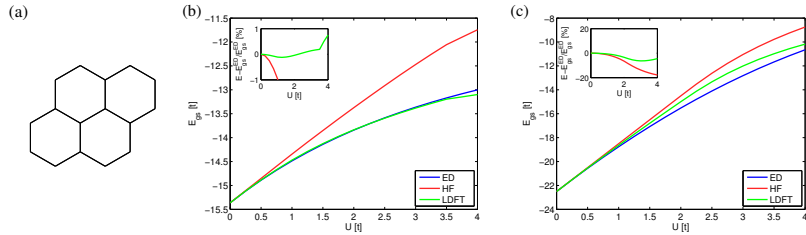
Figure 2.4. Comparing the LDFT model with exact diagonalization (ED) and the Hartree-Fock mean-field approximation (HF) (a) The structure of a 16-site graphene flake (b) A comparison of the ground-state energies at quarter-filling (c) Same as subfigure b but at half-filling. Insets show the deviation from the ground-state energy calculated using exact diagonalization in percentage.

filling, where the agreement is expected to be at its worst due to the fact that the agreement between the fitted e_{xc} and its exactly calculated counterpart is at its worst, the difference between the ground-state energies reduces to less than 5%, compared with the approximately 20% in Hartree-Fock calculation [Figure 2.4(c)].

Transferability of the model to inhomogeneous systems was demonstrated by adding an impurity site, modeled using an external potential. The LDFT ground-state energy stayed within 0.5% for the full range of the interaction, $U = [0, 4t]$. The validity of using only the lowest-spin polarization potential was tested by adding a spin-dependent impurity potential resulting in a strongly spin-polarized occupation in the solution calculated using exact diagonalization. Even in this case, the ED ground-state energy was closely reproduced using LDFT. This is somewhat surprising, as the exchange-correlation potential does not explicitly depend on the local spin imbalance.

Finally, it was verified that LDFT correctly predicts the high-spin ground states in triangular zigzag-edged flakes that arises from the sublattice imbalance between atomic sites belonging to the two sublattices according to the Lieb theorem [63], and also in the bow tie structure earlier studied by Wang *et al.* [12] using conventional DFT.

3. Graphene systems studied

3.1 Chemically modified graphene

Even though the linear band dispersion of graphene is beneficial for some applications, for instance the resulting constant optical absorption in the visible spectrum can be exploited in optical devices [15], in other applications such as transistors, a semiconducting band gap would be desirable. Lateral confinement can be used to open a gap in finite graphene nanostructures but an alternative means is to attach other chemical species to the carbon backbone, thus disturbing the π-electron system. Moreover, combining functionalized and pristine graphene regions might allow the preparation of full-carbon devices or circuitry.

In this Section, the functionalization of graphene using hydrogen and chlorine is studied with the density-functional theory. Section 3.1.1 introduces the methods of studying the structural stability of the different functionalized graphene systems. The results presented in Sections 3.1.2 and 3.1.3 are given in more detail in Publication II, Publication III, Publication IV and Publication V.

3.1.1 *ab initio* thermodynamics

Standard DFT corresponds to vacuum environment at the temperature 0 K. The relative stability of different functionalized graphene structures is compared by calculating the binding energy,

$$E_B = E_{\text{gra+func}} - (E_{\text{gra}} + n_{\text{func}}E_{\text{func}}), \tag{3.1}$$

where E_i is the DFT-calculated energy of species i, and n_{i} is the number of functionalizing units i in the functionalized system. In the thermodynamical sense, E_B corresponds to the internal energy of the system. Typically, the binding energy is calculated per functionalizing atom but it can also

be normalized with respect to surface area, or in the case of graphene nanoribbons, with respect to the unit length of the edge. This energy is called the edge formation energy E_F in Publication IV. Some care has to be taken when choosing the reference state used to calculate the binding energy. For diatomic molecules X_2 both atomic (X) and molecular (X_2) reference states are used in the literature. The actual values of E_B naturally depend on the chosen reference state, and when comparing with previously published values, only E_B calculated using the same reference state can be directly compared.

A realistic environment with gaseous surroundings can be taken into account by using *ab initio* thermodynamics [64], in which the internal energies corresponding to zero temperature are calculated using DFT but the results are extended to finite temperature and pressure using a classical entropy term. The feasibility of a structure or reaction at a finite (T, p) is dependent on the chemical potential of the functionalizing species. In the context of graphene, this approach has earlier been used to study the stability of different hydrogen-containing edge terminations of graphene nanoribbons [65].

The Gibbs free energy of the binding process, ΔG, as a function of the chemical potential of the functionalizing species, μ_x, is given by

$$\Delta G = E_B - \sum_i \rho_i \mu_i, \tag{3.2}$$

where i runs over all species involved in the process, ρ_i is the density of the functionalizing species. The chemical potential μ is given by $\mu = \mu_X^\circ(T) + kT \ln\left(\frac{P_X}{P^\circ}\right)$, with $\mu_X^\circ(T)$ is the standard chemical potential available in thermodynamical tables, such as Ref. [66], and P_X and P° are the partial pressure of species X and the standard pressure, respectively. Depending on the studied geometry, the density ρ_i may be an edge density or surface density. The reference states for the binding species used in all parts of the calculation must be consistent, i.e. if hydrogen adsorption is studied, either atomic hydrogen (E_H, μ_H) or molecular hydrogen (E_{H_2}, μ_{H_2}) can be used. If there are multiple binding species, two- or higher-dimensional stability diagrams can be calculated. The thermodynamically preferred structure has the lowest value of ΔG.

3.1.2   Graphane, hydrogenated graphene, on silicon dioxide

Silicon covered in thermal silicon oxide (Si/SiO$_2$) is one of the most widely used substrates for graphene. As SiO$_2$ is an insulator, the Fermi level of graphene can be shifted by gating. On the other hand, graphene flakes

can readily be identified exploiting optical contrast, allowing a quick and easy determination of the number of graphene layers [15]. The thermal SiO_2 surface is, however, rough, and local regions with different doping in graphene have been observed [28]. Moreover, the surface is amorphous.

Modeling non-crystalline materials using atomistic methods is challenging. In order to describe bulk systems instead of a cluster floating in vacuum, periodic boundary conditions have to be used. In DFT, the number of atoms in the simulation supercell is limited to the order of hundreds, and large-scale simulations with supercells capable of describing disorder and roughness on an experimental length scale are not possible. In practice, these factors make the study of a realistic SiO_2 surface unfeasible. Small periodic cells modeling crystalline SiO_2 in the α-quartz form can, however, be used to describe the local properties of the substrate. By considering different surface terminations, the inhomogeneity the surface is thus taken into account [67].

Graphane, freestanding hydrogenated graphene, was first theoretically proposed by Sofo *et al.* [68]. The change in the carbon hybridization from planar sp^2 to buckled sp^3 upon hydrogen adsorption was predicted to open a band gap. Subsequently, it was proposed that by selectively removing some of the hydrogen atoms, a conducting graphene nanoribbon within an insulating matrix could be formed [69]. Soon after the theoretical suggestion, hydrogen attachment onto SiO_2-deposited graphene was experimentally demonstrated, together with the observation of a small band gap in angle-resolved photoemission spectroscopy (ARPES) [30]. Other experiments using both metallic [70, 71] and insulating surfaces followed soon [30, 72–75]. Moreover, selective dehydrogenation was also achieved using a STM tip [73]. The observation of hydrogenated clusters on metal surfaces that were correlated with the Moiré pattern resulting from the lattice mismatch between the substrate and graphene suggested that the substrate might play a profound role in the hydrogenation process [75, 76].

The theoretical considerations, however, mainly addressed freestanding graphene hydrogenated from both sides, whereas the experiments [30, 70–75] studied substrate-deposited graphene. Thus, hydrogenation most likely occurred only from one side of the graphene plane. Theoretically, one-sided hydrogenation was found stable only for low hydrogen coverage in strongly corrugated graphene layers [77]. An understanding of the role of the SiO_2 substrate on the binding of hydrogen atoms to graphene on SiO_2 was lacking.

In Publication II and Publication III, the hydrogenation of graphene deposited on a SiO_2 substrate, modeled as a crystalline α-quartz phase,
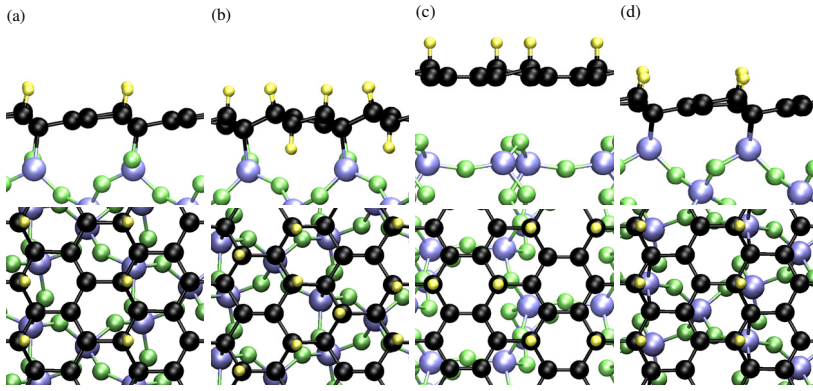
Figure 3.1. The lowest-energy hydrogenated graphene (graphane) structures on SiO$_2$ with different surface terminations. Top: side view, bottom: top view. (a) OT: 1/4 ML (b) OHT: 3/8 ML (c) ROT: 1/4 ML (d) SiT: 1/4 ML.

was studied. The effect of the surface termination on the stability of the resulting one-sided graphane was addressed in order to take into account the inhomogeneous nature of the surface, and its effect on the amount of hydrogen bound to graphene. Four different substrate terminations were studied in order to model different local regions: the oxygen-terminated (OT), the silicon-terminated (SiT), the hydroxyl-terminated (OHT) and the oxygen-terminated surface with a surface reconstruction (ROT) [67]. A commensurate structure with a low lattice mismatch of 1.3 % was formed from a 2×2 graphene primitive cell and a single hexagonal SiO$_2$ cell, and a large number of initial configurations for hydrogen coverages ranging from 1/8 to a full monolayer were considered. Long-range van der Waals interactions were taken into account within the Tkatchenko-Scheffler approach [78].

Figure 3.1 demonstrates the most stable graphane structures on the different SiO$_2$ terminations. Apart from the ROT surface, all surface terminations form chemical bonds to the hydrogenated graphene, and the lowest-energy coverages are below half a monolayer, 1/4-3/8 MLs. The hydrogen binding energy per carbon atom for all terminations and coverages is shown in Figure 3.2(a). In contrast to pristine graphene on the SiO$_2$ substrate, physisorbed at an equilibrium distance of approximately 3 Å, graphane is bound to the substrate through chemical bonds and the carbon backbone is consequently buckled. The buckled structure resembles the structure of freestanding graphane as predicted by Sofo *et al.* [68]. Only on the least reactive ROT surface, the lowest-energy structure does not bind to the uppermost substrate atom by chemical bonds but is, instead, physisorbed [Figure 3.1(c)]. This structure was, however, found to
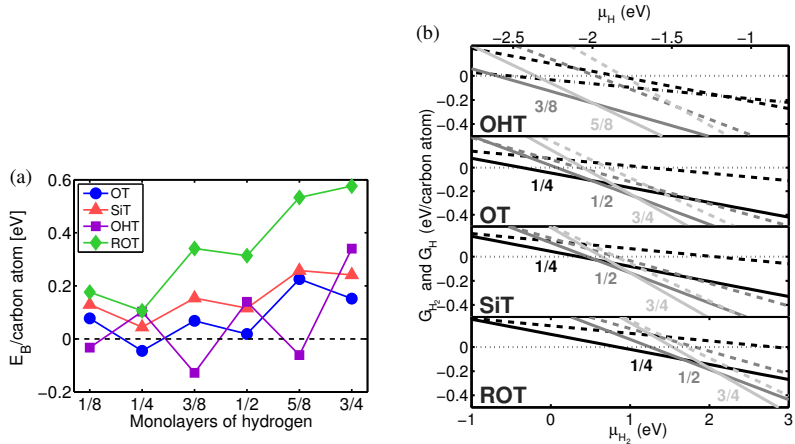
Figure 3.2. The stability of SiO_2-deposited graphane (a) The binding energy per carbon atom for different hydrogen coverages on the four SiO_2 surface terminations (b) The Gibbs free energy of formation (G_{H/H_2}) for the lowest-energy hydrogenated structures at hydrogen coverages 1/8–3/4 monolayers as a function of the chemical potential μ of H_2 (lower x-axis) and atomic H (upper x-axis). The favored structure is the one with the lowest ΔG, and the corresponding coverages (in monolayers, MLs) are indicated below the curves.

be unstable against H_2 desorption, as seen from a positive binding energy with respect to molecular hydrogen [Figure 3.2(a)]. The local structure of the substrate thus has a profound effect on the stability of hydrogen adsorption. Hydrogenation was found to be most energetically favored on the hydroxyl-terminated surface, as the hydrogen atoms from the OH groups are able to stabilize the structure by binding to graphene from below [Figure 3.1(b)]. The resulting structure thus resembles freestanding graphane.

The effect of the hydrogen content in the environment was addressed using *ab initio* thermodynamics. It was found out that even at high pressures and temperatures corresponding to large chemical potentials, molecular hydrogen might not be reactive enough to hydrogenate graphene. Instead, with atomic hydrogen, the hydrogen pressure could possibly be used to control the hydrogen coverage. This is illustrated in Figure 3.2(b) showing the Gibbs free energy of the binding process, ΔG, as a function of the chemical potential of the hydrogen species, μ_{H/H_2}. The chemical potential scale is shown both for atomic (H) and molecular hydrogen (H_2). In terms of E_B, the hydroxyl-terminated surface with 3/8 ML coverage is the most stable one. Changing the amount of hydrogen in the gas phase, especially if hydrogen is in atomic form, might allow the formation of other coverages but the one with the lowest E_B, as well as allow thermodynamically stable graphane structures on other surface terminations. Kinetic
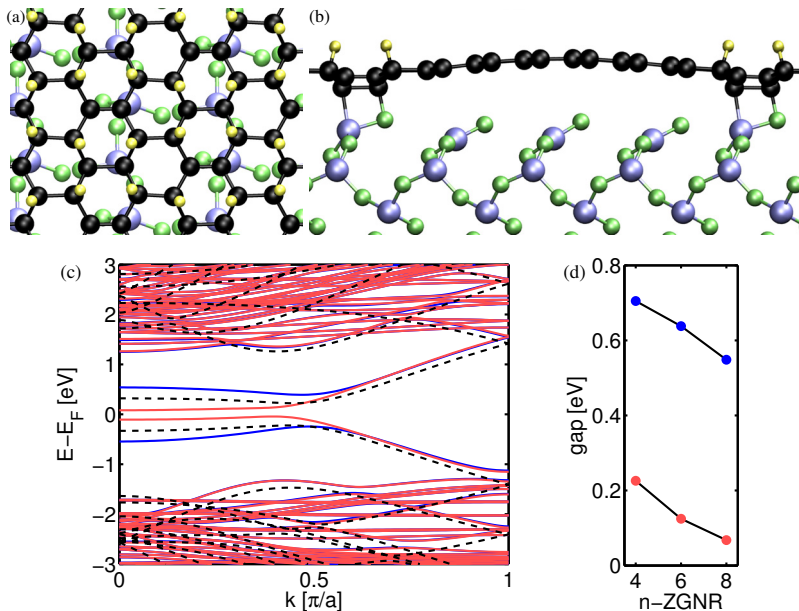
Figure 3.3. The structure and electronic properties of graphene nanoribbons formed by dehydrogenating SiO_2-deposited graphane. (a) The hydrogenation pattern on the OT surface with 1/2 ML hydrogen coverage. (b) A 6-ZGNR in graphane matrix (1/2 ML coverage), side view. (c) The band structure of the 6-ZGNR. Dashed lines show the bands of a freestanding hydrogen-terminated ribbon, and blue and red denote the two spin channels of the ribbon on SiO_2 in the graphane matrix. (d) The band gaps for both spin channels as a function of the ribbon width.

factors might prevent or at least slow down desorption processes when the sample is transferred to a normal ambient environment.

Even though the idea of forming graphene nanoribbons in a graphane matrix had already been proposed [69], the effect of substrate-induced asymmetry on their electronic properties such as the band gap had not been addressed before Publication III. Figure 3.3(a) shows the structure of graphane with 1/2 ML hydrogen coverage on the OT surface and Figure 3.3(b) shows a side view of a zigzag nanoribbon formed in it. Even though in terms of binding energy this hydrogenation pattern was not found to be the most stable one, tuning the reaction conditions might allow its formation as illustrated in Figure 3.2. No ribbons with well-defined armchair edges could be formed at any hydrogen coverage in the substrate-deposited graphane structures.

The distance between the carbon atom and the uppermost substrate atoms is different for graphene and graphane. Upon hydrogenation, the distance decreases from approximately 3 Å to slightly below 2 Å. Consequently, the ribbon region is slightly bent upwards with respect to the graphane matrix. This small curvature does, however, not appear to have

a significant effect on the electronic properties of the ribbon. The zigzag edges are spin-polarized and a gap opens in the flat band, similar to free-standing ribbons [46]. The two edges of the nanoribbon become, however, non-equivalent due to the asymmetry of the substrate below with respect to the ribbon axis. This leads to different couplings between the spin-polarized edge states and the substrate for the two spin species localized at the opposite ribbon edges. The band structure is modified accordingly, so that the spin up and down species have a different band gap as shown in Figure 3.2(c). With an increasing width of the ribbon, both gaps decrease. Figure 3.2(d) shows the band gaps for the ribbons widths accessible using the present computational approach. For a wide enough ribbon, too large to be simulated, a half-metallic band structure with one of the spin channels being metallic and the other having a band gap might be reached. Previously, external field has been suggested to turn zigzag ribbons half-metallic [46].

3.1.3   Interaction between graphene and chlorine

After the successful hydrogenation experiments, interest in functionalizing graphene with other chemical species and thus selectively modifying its electronic and mechanical properties increased. Soon after the first graphane experiments, the fluorination of graphene was demonstrated [31, 32, 79]. The fluorination was found to occur stoichiometrically [31, 32], and the resulting insulating fluorographene was predicted to be more stable than graphane [31, 80]. Thermal defluorination was also successful but it was also found to induce defects to the graphene backbone [79]. Calculations on fluorographene structures agreed quite well with the experiments, both in terms of the predicted covalent-type bonding between the carbon and fluorine atoms and stability [31, 79, 81]. The preferred attachment of fluorine to defected regions was, however, also suggested [80]. Overall, the functionalization of graphene using fluorine seemed to be quite similar to that using hydrogen.

The attachment of chlorine atoms to graphene was not demonstrated experimentally until 2011 [82]. This might have been partly because theoretical studies predicted that chlorine would not bind covalently to graphene sp^2 carbons, but, instead, adsorb through long-range forces with carbon-chlorine distances around 4 Å [81, 83]. Moreover, these stoichiometrically chlorinated graphene sheets were predicted to be unstable [81]. Studies on the interaction between single chlorine atoms [84, 85] or Cl_2 molecules [86] and graphene also failed to find chemical binding. Later,

some stable structures with full or half chlorination have, however, been reported based on DFT calculations [87, 88].

In the first chlorination experiment [82], Cl_2 molecules were split into Cl radicals using light. Subsequently, they were allowed to react with SiO_2-deposited graphene. After the reaction, sp^3 carbon-chlorine bonds were observed in X-ray photoemission spectroscopy. Additionally, the amplitude of the Raman D peak increased, indicating the formation of defects of some kind, and the presence of nanodomains approximately 30-50 nm in lateral dimension was observed. Few months later, Wu *et al.* [89] used Cl_2 plasma to chlorinate graphene. For short exposure times, they found only a reversible effect on doping and Raman spectrum, in accordance with the theoretical predictions for weak binding. For longer exposure times, an irreversible change occurred, associated with the formation of patches with attached Cl.

The first experiment with the observed nanodomains [82], in particular, raised the question whether chlorine might actually prefer to bind to graphene edges, or even induce the formation of defected regions or edges. In Publication IV, the binding of Cl atoms both to the basal plane of graphene and to graphene edges modeled with graphene nanoribbons was studied. In order to distinguish between the reaction conditions, characterized by the presence of radical Cl, and ambient conditions, in which the formation of Cl_2 molecules is possible, both Cl and Cl_2 were used as the reference states when calculating the binding energies. Experimentally, chlorinated graphene was found to be stable also in ambient conditions [82]. Both for armchair- and zigzag-terminated nanoribbons, a large number of chlorine-containing edge terminations was considered. In general, chlorinated armchair edges were found to be more stable than their zigzag-terminated counterparts, and in the most stable configurations, chlorine atoms replaced hydrogen atoms in the most stable edge hydrogenation patterns (zigzag: H-H-H_2 alternation of the edge carbon hydrogenation, armchair: H_2) [65]. Figures 3.4(a) and 3.4(b) illustrate the studied edge terminations, as well as show the chlorine binding energy and the edge formation energy for each of them. It was found that the binding of Cl to graphene edges is preferred over Cl adsorption onto the basal plane. Moreover, some of the chlorinated edges are stable even in ambient conditions.

Furthermore, the possibility of chlorine-induced edge formation in the photochlorination experiment was addressed using *ab initio* thermodynamics. The resulting stability diagrams as a function of the chemical potential for both atomic (Cl) and molecular (Cl_2) chlorine are shown in
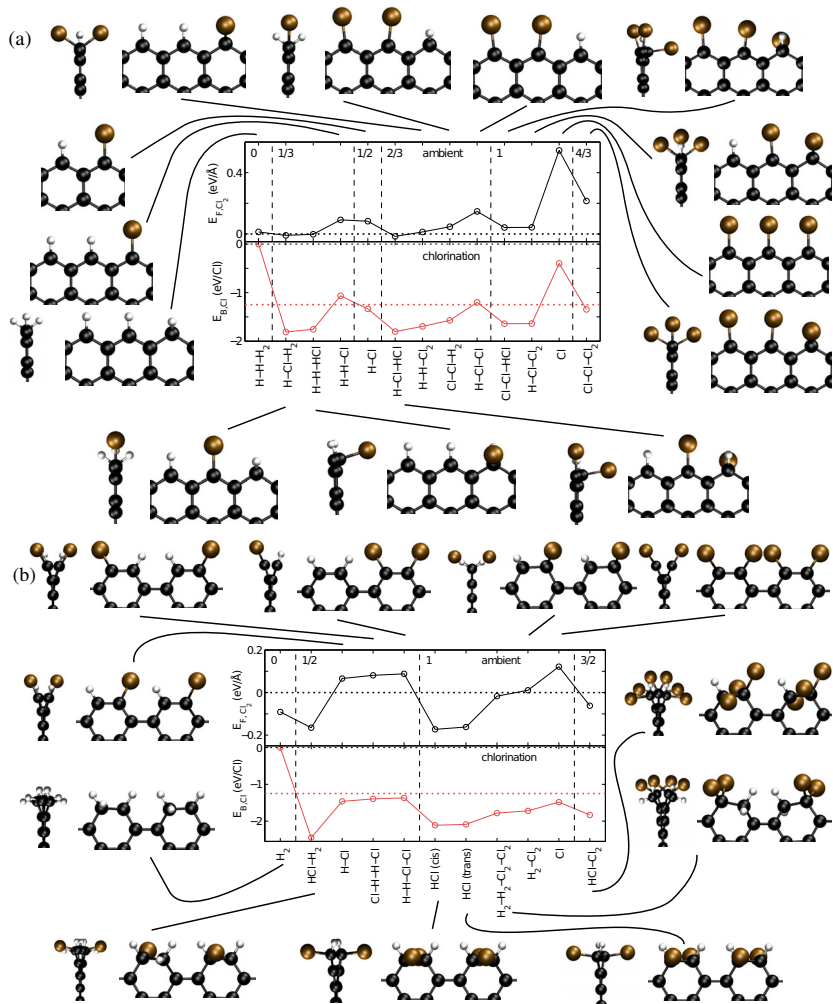
Figure 3.4. The stability of different chlorine-containing graphene edges. (a) Zigzag edges (b) Armchair edges. Upper panels: edge formation energy E_{F,Cl_2}, lower panels: chlorine binding binding energy $E_{B,Cl}$. In the upper panels, the dotted horizontal line at zero energy denotes pristine graphene used as the reference, and in the lower panel, the dotted line shows the adsorption energy of a single Cl atom on graphene. Structures connected to the middle graph from (above) below are (un)stable in ambient conditions. Vertical dashed lines separate groups of different degrees of edge chlorination, expressed in chlorine atoms per edge carbon atom.
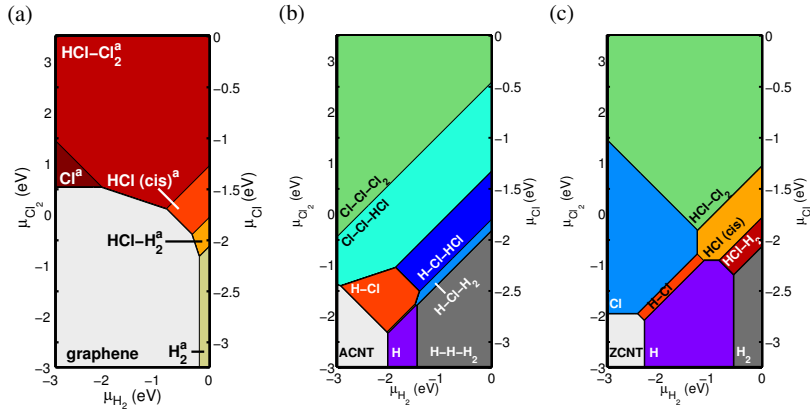
Figure 3.5. The stability diagrams of different chlorinated edges as a function of the chemical potential of hydrogen and chlorine. For Cl, the scales for both atomic and molecular reference states are given. The carbon reference state is (a) graphene (b) armchair nanotube (5-ACNT) (c) zigzag nanotube (8-ZCNT). In (a), both armchair and zigzag edges are allowed. In (b) and (c), longitudinal unzipping is assumed, and thus only zigzag and armchair edges are possible in (b) and (c), respectively.

Figure 3.5(a). The nomenclature of the different edges is shown in Figure 3.4, and the superscript "a" or "z" indicates whether the edges are of armchair or zigzag type, respectively. Given that the chemical potentials of chlorine and hydrogen are high enough, chlorine-containing armchair edges are energetically preferred over pristine graphene.

If chlorine might induce edge formation in graphene, the same might be possible in carbon nanotubes as they are less stable than graphene due to the curvature-induced strain. Oxidative reagents have been experimentally found to be capable of longitudinally opening nanotubes, yielding graphene nanoribbons rich in oxygen-containing functionalizing groups [26]. Preparing GNRs by unzipping nanotubes has the advantage that the size and chirality of the original tube determine the width and edge termination of the resulting GNR. Thus, for longitudinal opening, zigzag nanotubes (ZCNT) open into armchair nanoribbons (AGNR), and vice versa. In addition to oxidative reagents, also hydrogen and fluorine have been suggested to be capable of tube unzipping [90–92]. Similar to the original oxidative unzipping, in experiments, these yield surface-functionalized ribbons [93, 94]. It would thus be of interest to find a reagent that could unzip CNT but that would not be capable of functionalizing the basal plane of the resulting ribbons.

The possibility of using chlorine as such a reagent was studied in Publication V. As shown in Publication IV, the binding of chlorine to the graphene basal plane is not preferred, and chlorine desorbs from it in am-
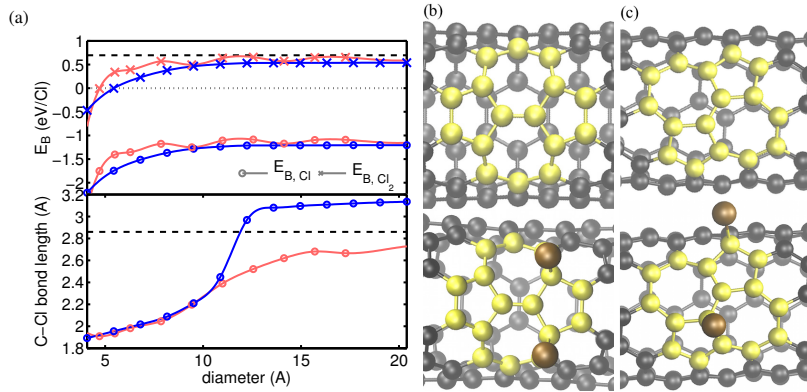
Figure 3.6. The binding of Cl to carbon nanotubes (a) The Cl binding energy (upper panel) and C-Cl bond length (lower panel) as a function of nanotube diameter. Red: zigzag nanotube, blue: armchair nano tub. The lines are a guide for the eye. The dashed lines show the values for planar graphene with a comparable Cl-Cl separation, and circles and crosses denote radical (Cl) and ambient (Cl$_2$) reference conditions in the upper panel. (b),(c) Two non-equivalent orientations for the Stone-Wales defect in a 5-ACNT. Top: defect in the absence of chlorine, bottom: The most stable two-chlorine configurations

bient conditions. In the large-diameter limit, the properties of the CNTs approach those of graphene. This is well illustrated in Figure 3.6(a), in which the binding energy and carbon-chlorine bond length for chlorine adsorption are shown as a function of tube diameter, both for ZCNT (red) and ACNT (blue). With an increasing diameter, the binding energies approach the graphene limit. In armchair tubes, there is a clear crossover in the C-Cl bond length around the diameter 12 Å. This is related to a change in the preferred chlorine adsorption position from the chlorine atom being on top of a carbon atom to being on a bridge site between two carbon atoms along the tube circumference. The periodic modulation seen in the case of ZCNT is due to the diameter-dependent alternation of metallic and semiconducting ZCNT, similar to armchair nanoribbons.

Figures 3.5(b) and 3.5(c) show the thermodynamical stability diagrams for unzipping 5-ACNT and 8-ZCNT, respectively. As longitudinal unzipping yields GNRs of only one edge termination, the superscripts "a" and "z" are not shown. It is seen that the region of the (μ_{H_2}, μ_{Cl/Cl_2} space, within which the pristine nanotube is preferred over chlorine-containing edges is much smaller than in the case of graphene [Figure 3.5(a)]. With an increasing tube diameter, the size of this region grows and again approaches the graphene limit. Depending on the chemical potentials of the chlorine and hydrogen species, a large number of differently terminated edges are possible. Similar to graphene chlorination, if the chlorine content of the environment is high enough, ribbons with a dense chlorination

at the edges are preferred over unzipped pristine nanotubes. Moreover, by controlling the amount of hydrogen and chlorine in the environment, as well as the reaction temperature, tubes with a diameter smaller than a threshold value might be opened.

In addition to tube unzipping, the effect of Stone-Wales defects on the energetics of Cl adsorption was studied in Publication V. This is relevant for unzipping, as defects might act as nucleation sites for the process. Figures 3.6(b) and 3.6(c) illustrate two non-equivalent orientations of a Stone-Wales defect in a 5-ACNT. The Cl binding energy on each of the non-equivalent sites belonging to the defect was calculated. It was found out that, as expected, the defect sites are more reactive than pristine tubes. Additionally, the functionalization preferably occurs at carbon atoms belonging to bonds that are oriented nearly along the circumference of the tube. A comparison between a Stone-Wales defect in pristine graphene and in nanotubes showed that in graphene, only a single Cl atom could be bound to the defect, while in nanotubes the binding of multiple chlorine atoms was feasible. Even though the binding of Cl atoms was preferred on the defects, no direct evidence was found for Stone-Wales defects acting as unzipping nucleation centers.

3.2 Atomically well-defined graphene nanoflakes on metal substrates

The interface between graphene and monocrystalline metal surfaces is atomically smooth, apart from step edges, and the effects of disorder are much less significant than on thermal SiO_2. Metals can be divided into two groups based on the strength of the interaction between the surface and graphene to those that form chemical bonds with graphene, such as Co and Ni, and to those on which graphene physisorbs, such as Au and Pt [95–97]. If the interaction between graphene and the surface is weak, it does not destroy the linear dispersion at the corners of the Brillouin zone. The substrate may, however, dope graphene, causing the Fermi energy to shift with respect to the conical points. In the case of strong, chemical interaction between the topmost surface atoms and graphene carbon atoms, the electronic structure is strongly modified, and the conical dispersion may be destroyed [95, 96, 98].

It appears, however, that DFT-based studies of graphene on metal surfaces are extremely sensitive to the choice of the exchange-correlation functional, as well as the choice of the supercell and the way the metal

surface and graphene unit cells are made commensurate [99]. In general, calculations within LDA tend to overestimate the binding energy and underestimate the equilibrium distance [97, 100]. PBE, on the contrary, greatly underestimates the binding strength and overestimates the equilibrium distance between the metal surface and graphene [97]. The effect and importance of van der Waals forces for the binding on different metals is being debated. In theoretical calculations, the bonding strength appears to depend on the chosen van der Waals approach, as both weak binding on all metal surfaces [100] and the division into the two metal categories have been reported [76, 98]. More recently, the random phase approximation (RPA) has been used to study metal-graphene interfaces [97]. Even though the RPA-calculated equilibrium distances seem to reproduce the experimentally observed division into weakly and strongly interacting metals, with an improved description of the binding energies [97], it is clear that the interfaces still remain an interesting topic of theoretical study.

Depending on the lattice constant and the surface termination of the metal, large-scale Moiré patterns resulting from the interference of the mismatched lattices of graphene and the substrate are observed in metal-deposited graphene. The periodicity of Moiré is not only dependent on lattice mismatch, the difference in the length of the primitive vectors of the surface and of graphene, but also on their relative orientation with respect to each other. Even on the same substrate different Moiré periodicities can be observed for different twist angles between the graphene and substrate lattices. The presence of a Moiré may lead to, for instance, a modulation in substrate-graphene distance or doping [101–104].

In finite graphene nanostructures on metal surfaces, the edges are more reactive than the interior of the graphene flake, and thus they may bind to the substrate, bending towards it [105]. The large edge-surface ratio in graphene nanoflakes might markedly change their properties such as doping compared with large-scale graphene on the same surface.

In this Section, graphene nanoflakes formed either by chemical vapor deposition on Ir(111), [Publication VI], or bottom-up synthesis on Au(111), [Publication VII], are studied. The experimental scanning tunneling spectroscopy (STS) measurements, performed by collaborators at Aalto University and Utrecht University, are compared with theoretical calculations using the tight-binding model or density-functional theory. Section 3.2.1 introduces STS and how to model it, and Sections 3.2.2 and 3.2.3 present the main results of the joint experimental-theoretical studies of Publication VI and Publication VII. Additionally, the electronic

structure of finite armchair GNR corresponding to the experiments in Publication VII is studied in Publication VIII, concentrating on the effect of doping and defects on the electronic states localized at the zigzag termini of the ribbons.

3.2.1 Scanning tunneling spectroscopy

In scanning tunneling microscopy (STM) and spectroscopy (STS), a conducting tip is brought close to a conducting surface and a bias voltage is applied between them. Consequently, tunneling through the vacuum barrier occurs. If a molecular system is deposited on the surface, the electronic properties of the composite molecule-substrate system are probed. Figure 3.7 shows the setting for a triangular graphene flake deposited on a gold surface, probed by a CO-terminated gold tip. The current between the probe and the surface is recorded, and the differential conductance signal, dI/dV can be obtained either by numerical derivation of the current signal when scanning the bias, or by periodic modulation of the bias voltage around a chosen value. In the first approximation, this signal probes the local density of states (LDOS) of the whole sample, thus directly probing its electronic properties [106]. If the coupling between the nanostructure and the substrate is weak, it may be possible to directly probe the electronic states of the nanostructure. This can be achieved, for instance, by covering the substrate with few atom layers of an insulating material before depositing the nanostructure [107]. dI/dV spectra can be recorded by fixing the tip position and changing the bias, whereas dI/dV maps are obtained by fixing the bias and scanning the tip position across the sample.

In order to simulate STS-measurements, it is thus necessary to be able to calculate the LDOS of the studied system. The local density of states can be calculated from the eigenvalues ϵ_n and wave functions $|\Psi_n\rangle$, given by DFT or lattice models, as

$$\frac{dI}{dV}(\vec{r}, V) \propto \rho(\vec{r}, E) = \sum_n |\langle \vec{r}|\Psi_n(\vec{r})\rangle|^2 \, \delta(E - \epsilon_n). \qquad (3.3)$$

In practice, the delta peaks at the orbital energies are not observed in experiments. A finite temperature, the coupling between the nanostructure and the substrate, and instrumental precision may broaden the experimental peaks. Consequently, in the simulation the delta peak is broadened into a Lorentzian,

$$\delta(\epsilon) \to \frac{\eta}{\epsilon^2 + \eta^2}. \qquad (3.4)$$

Here, η gives the width of the broadening. If a lattice model is used to
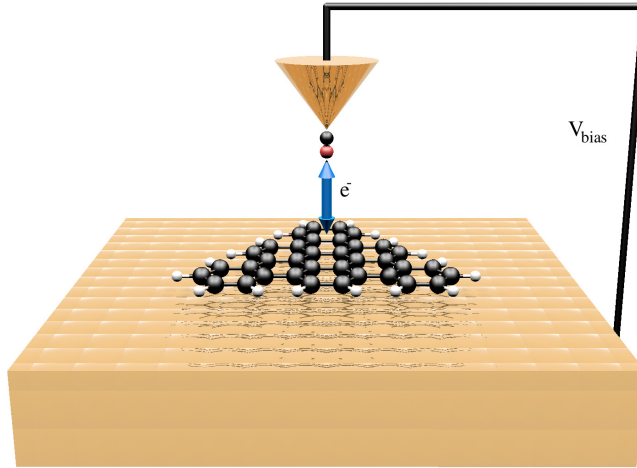
Figure 3.7. An illustration of the experimental setup for a scanning tunneling spectroscopy measurement. A bias voltage V_{bias} is applied between the substrate and the tip that can also be terminated with a molecule, such as CO illustrated in the figure. The studied nanostructure is deposited on the substrate, and depending on the bias voltage, electrons tunnel over the vacuum barrier from the substrate to the tip or vice versa.

calculate the electronic states, the continuous location variable $\vec{r}$ is discretized and defined only on the lattice sites. In order to simulate realistic real-space dI/dV maps, the calculated LDOS defined on the lattice has to be expanded, for instance by placing analytical carbon atom p_z orbitals [108] on each of the lattice sites.

In the Tersoff-Hamann model [106], spherical s-wave symmetry was assumed for the tip when simulating STM measurement. This corresponds rather well to metal-terminated tips but in experiments, also small molecules may accidentally or intentionally be attached to the tip. For example, Gross *et al.* [109] studied pentacene and naphthalocyanine adsorbed on copper, and showed that the STM images obtained using a CO-terminated tip were not described well using the s-wave approximation. Instead, simulations using a tip with a mixed s- and p-wave character matched the experiments. The original STM theory was extended to more complicated tip symmetries, such as p- and d-wave tips, by Chen [110]. The expression for the dI/dV signal has to be modified accordingly, to

$$\frac{dI}{dV}(\vec{r}, V) \propto \sum_n M_\alpha(\Psi_n(\vec{r}))\delta(\epsilon_n - eV). \tag{3.5}$$

Here, $M_\alpha(\Psi_n(\vec{r}))$ is the tunneling matrix element whose functional form depends on the tip symmetry. Eq. (3.5) reduces to the original Tersoff-Hamann expression in the s-wave case with $M_s = |\langle\vec{r}|\Psi\rangle|^2$. The tunnel-
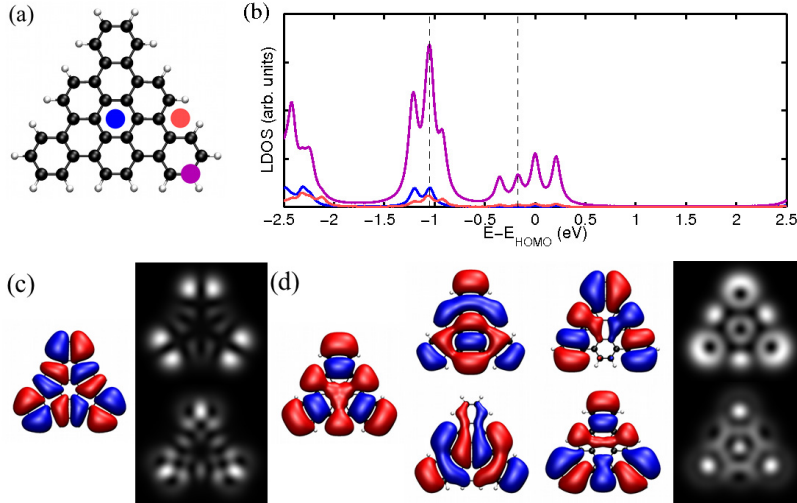
Figure 3.8. A STS simulation. (a) The atomic structure of a 36-carbon atom armchair triangle. The colored circles mark the spots on which the STS spectra shown in subfigure b are calculated. (b) The simulated dI/dV curves using a s-wave tip at the height 3.5 Å above the carbon layer, with broadening $\eta = 0.05$ eV for a hole-doped triangle (charge $q = 2$). The colors correspond to the locations shown in subfigure a, and dashed lines indicate the energies of the STS maps in subfigures c and d. (c),(d) Right: STS maps calculated at $E = -0.17$ eV and -1.05 eV, marked with dashed lines in subfigure b. Top: s-tip. Bottom: p-tip (equal weight for p_x and p_y). Left: the contributing molecular orbitals.

ing matrix elements for other tip symmetries can be calculated using the simple derivative rule by Chen [110]. For instance, p_x symmetry of the tip results in $M_{p_x} = \left| \langle \vec{r} | \frac{\partial \Psi}{\partial x} \rangle \right|^2$, and a spherically symmetric p-wave tip [109] corresponding to the symmetry of a CO molecule is obtained as $M_{p_x} + M_{p_y}$.

In addition to a broadening in energy, the finite size of the tip should also be taken into account. In the original work of Tersoff and Hamann [106], a point-like tip was assumed. One method of taking the finite size of the tip into account in modeling topographic dI/dV maps is to use the rolling ball method, in which the tip trajectory is simulated by considering the path of a ball with a given radius moving on the surface of the sample. A simpler approach is to use Gaussian blur, and in the present work, it was used to modify the tunneling matrix element when simulating the dI/dV spectra for a fixed tip position. Thus, the tunneling matrix element of Eq. (3.3) was broadened using a Gaussian,

$$\hat{M}_i(\vec{r}) = \int_{S(\vec{r})} M_i(\vec{r'}) e^{-\frac{(\vec{r}-\vec{r'})^2}{\sigma}} d\vec{r'}. \tag{3.6}$$

where σ gives the width of the broadening.

To illustrate a STS simulation in practice, Figure 3.8 shows a STS simulation for a triangular hole-doped (charge $q = 2$) armchair-edged graphene flake consisting of 36 carbon atoms [The structure is illustrated in Fig-
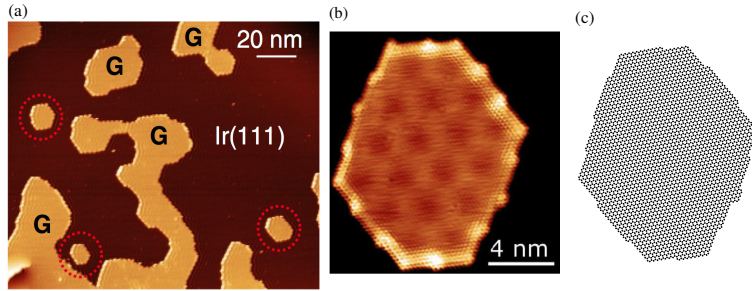
Figure 3.9. CVD-grown graphene flakes on Ir(111). (a) A STM image showing an overview of the sub-monolayer graphene coverage with graphene flakes of different shape and size. (b) A close-up view of one of the flakes studied. (c) The atomic model determined for the same flake.

ure 3.8(a)]. Figure 3.8(b) shows the simulated dI/dV signal using an s-tip at three different positions on the structure 3.5 Å above the plane of the carbon atoms, marked with colored dots in Figure 3.8(a). The different magnitudes are related to tip positions being directly on top of a carbon atom (purple) or at a hollow site in the middle of a carbon hexagon (red, blue). Figures 3.8(c) and 3.8(d), respectively, illustrate that the patterns observed in dI/dV maps can result either from a single molecular orbital or from multiple states lying close to each other in energy. This was found to be of uppermost importance in Publication VI, in which matching the experimentally measured dI/dV maps required the mixing of close-lying eigenstates through energy broadening. Additionally, the difference between s- and p-symmetry tips on the dI/dV maps is demonstrated.

3.2.2 Quantum-confined states in zigzag-edged graphene islands on Ir(111)

Chemical vapor deposition (CVD) on transition metal surfaces is a widely used method of synthesizing large-scale graphene sheets. Albeit, graphene synthesized using CVD is not single-crystalline as there are a large number of nucleation centers from which the growth proceeds. By controlling the synthesis conditions, the graphene coverage can also be restricted to less than a monolayer, thus forming graphene quantum dots (GQDs). Using postannealing, the original shape of the flakes, roughly hexagonal, can be to some extent controlled [21].

In Publication VI, scanning tunneling spectroscopy and microscopy were used to study CVD-synthesized GQDs on Ir(111). Measuring the dI/dV spectra and maps allows one to study both the nodal pattern of the LDOS and the energies of the quantum dot electronic states with respect to the Fermi level of the substrate-graphene system. High-quality STM topo-
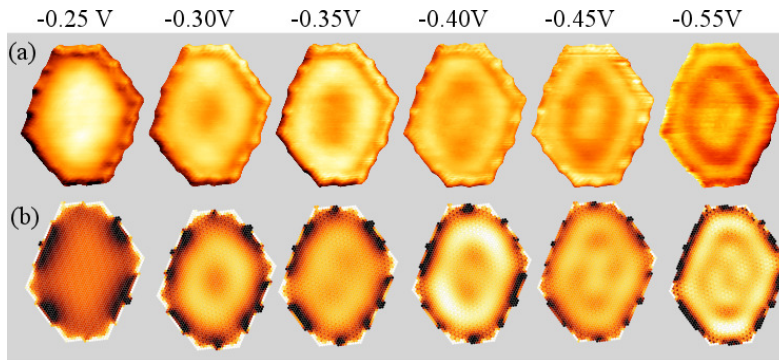
Figure 3.10. Quantum-confined states in Ir(111)-deposited graphene flakes (a) Experimental measurements, bias voltage indicated. (b) Local density of states at corresponding energies calculated from a scaled tight-binding model.

graphic images allow the determination of the atomic structure of the GQDs on the level of single atoms.

Figure 3.9(a) shows an overview of the experimentally prepared flakes. The flake edges are, in general, of zigzag termination, but kinks of one or two carbon rows appear at the edges. The distance between the kinks is correlated with the wavelength of the Moiré pattern between the graphene and Ir(111) lattices, as seen in Figure 3.9(b) showing a close-up view of a flake with darker and brighter regions resulting from the Moiré. Using high-resolution experimental STM images, the atomic positions for the carbon atoms forming the flake were determined [Figure 3.9(c)].

When scanning the bias voltage, confined states with spatial patterns resembling standing waves were observed. The first state below E_F has a maximum in the middle of the flake, the second state a node, the third two maxima and a node, and so on. Figure 3.10(a) shows the experimental measurements at the energies with clearly distinguishable nodal patterns. These patterns cannot arise from single eigenstates, even though this has been suggested in the literature [111]. The number of atoms in the flake is of the order of thousands [The structure of the flake is illustrated in Figure 3.9(c)], and thus the spacing between energy levels is much smaller than the energy separation between the different nodal patterns. The patterns were, instead, found to result from the broadening-induced combination of multiple electronic states with small energy spacing, in the fashion of Figure 3.8(d). Figure 3.10(b) shows the LDOS maps simulated using the tight-binding model. The spatial broadening is taken into account by averaging the LDOS over the six carbon atoms of each hexagon. By scaling the tight-binding parameters using a constant factor, a one-to-one correspondence between the experimental and simulated

energies was established. The scaling of the parameters corresponds to a change in the slope of the linear bands at the corner of the Brilloiuin zone, which in turn defines the Fermi velocity. The good agreement between the experiment and the simulation using the tight-binding model demonstrates that the coupling between Ir(111) and graphene is weak enough, so that modeling freestanding graphene is sufficient. Moreover, as the tight-binding model implicitly contains electron-electron interaction on the mean-field level, interaction effects are either not very important, or they are screened by the substrate.

It is worth noting that, in contrast to the simulated LDOS maps [Figure 3.10(b)], the edges of the graphene flakes are not bright in the experiment [Figure 3.10(a)]. This absence of the theoretically predicted zigzag edge states is most likely due to the interaction between the edge and the substrate that causes bending of the edge toward the substrate [105].

The Fermi velocity in graphene flakes on Ir(111) was determined from the scaled tight-binding parameters, and also from the experimental measurements by correlating the experimental energies of the confined states with simulations using the Klein-Gordon equation. The determined value of the Fermi velocity $v_F = 6.2 \cdot 10^5$ m/s was, however, lower than the typical value for freestanding graphene, $v_F = 10^6$ m/s [7]. This discrepancy might be due to finite-size effects and averaging of the slope of the Fermi cone with respect to different directions in the k-space. As Fermi velocities of $6.5 \cdot 10^5 - 9.2 \cdot 10^5$ m/s have been reported for large-area graphene on Ir(111) [112–114], the reduction is, however, most likely predominantly due to interaction with the substrate, leading to screening of interactions and to a decrease in the slope of the dispersion.

Almost simultaneous reports on the quantum-confined states in Ir(111)-deposited GQDs were published by other groups [111, 115, 116], in addition to Publication VI. Each of the papers presented a slightly different interpretation on the nature of the confined states, with different theoretical approaches used to model the confined states. Phark *et al.* [115] were the first ones to publish an all-experimental study on the topic, extracting a Fermi velocity in close agreement with Publication VI ($v_F = 6.3 \pm 0.40 \cdot 10^5$ m/s). The reduced Fermi velocity was explained to result from graphene-substrate interaction, as well as from graphene edges acting as extended lattice defects.

Subramaniam *et al.* [111] attributed the nodal structure of the dI/dV maps to individual single-particle eigenstates of the flakes, and simulated them using the tight-binding model. In order to account for the discrepancy between the asymmetric theoretical eigenstates arising due to the

kinks at the flake edges, and the rather smooth and symmetric experimental maps, they used a softened confinement potential in the tight-binding simulation. In addition to this potential describing the bending of the edges toward the substrate, they also explicitly included the Moiré superlattice potential. The Fermi velocity determined using this approach was even lower then in Publication VI and Ref. [115], namely $v_F = 4.5 \cdot 10^5$ m/s. This was explained to result from the intrusion of the Ir(111) surface state into graphene.

Last, Altenburg *et al.* [116] attributed the observed confined states completely to the Ir(111) surface state that is locally gated by the graphene islands. Using DFT calculations on the pristine as well as graphene-covered Ir(111) surface, they argued that, at the Fermi energy, the Ir(111) surface state is at the Γ point whereas the graphene states are at the K point in the Brillouin zone. Consequently, an electron tunneling from the tip can only tunnel to the iridium surface state as tunneling to graphene states would require a change in the electron momentum. By simulating the STM measurements using the Tersoff-Hamann method [106] in the bulk system, they found that the Ir states contributed more to the tunneling current than graphene states. They base their arguments, however, on a bulk theory. In finite flakes, the Brillouin zone is folded onto the Γ point and their argument on the wave vector mismatch is unlikely to apply.

3.2.3   Finite-length armchair nanoribbons on Au(111)

The bottom-up graphene synthesis was introduced in 2010 in the seminal paper by Cai *et al.* [23], who demonstrated the on-surface polymerization of 10,10'-dibromo-9,9'-bianthryl precursor molecules into seven carbon rows wide armchair nanoribbons, 7-AGNRs. The advantage of the method was that, in contrast to etched GNRs, the structure of the ribbon edge carbon atoms was known with atomic precision. Figure 3.11 illustrates the structure of the precursor molecule, as well as a three-monomer GNR. In addition to these straight ribbons, Cai *et al.* [23] also demonstrated the synthesis of chevron-type structures, as well as three-arm junctions between them. Later, the bottom-up synthesis of 7-AGNRs has also been demonstrated using Ag(111) [23, 117] and Au(788) [118] as the substrate. The shape of the synthesized graphene is limited by the available precursor molecules but at least armchair-edged triangular graphene flakes on Cu(111) have been prepared [24].

This new synthesis method started a surge in investigations on 7-AGNRs. Their electronic structure [118–122], transport properties [121], as well
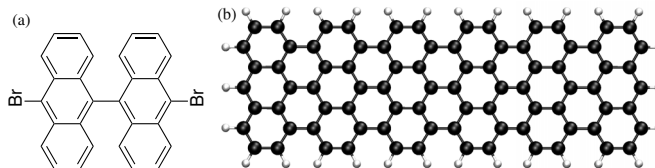
Figure 3.11. Bottom-up synthesis of graphene nanoribbons (a) The precursor molecule used to synthesize the finite nanoribbons in Publication VII. (b) The structure of a three-monomer long ribbon.

as the detailed mechanism of the on-surface polymerization step [123, 124] have been addressed. The presence of states localized to the zigzag termini close to the Fermi level analogous to the edge states in zigzag nanoribbons was revealed. The nodal patterns of these states in the dI/dV maps match the simulations well [120, 121]. Actually, termini with different nodal patterns were observed in the experiments. They were attributed to a quenched edge state due to a double hydrogenated zigzag carbon atom at the terminus and to a precursor bromine atom that wasn't detached during the polymerization process [121]. Theory predicts that the zigzag edge states of zigzag nanoribbons should split in energy due to an antiferromagnetic coupling between the individually ferromagnetic edges [46]. This has, however, not been observed for finite ribbons.

In Publication VII, on-surface synthesized finite 7-AGNRs were studied using simultaneously measured atomic force microscopy (AFM) and STS. Using a CO-terminated tip, the atomic structure of the ribbons, as well as possible structural imperfections, were imagined in AFM at high precision. Interestingly, a previously unobserved feature was seen in the STS spectra recorded at the zigzag-terminated ends. The end-state peak at positive bias was found to split into two subpeaks separated by 0.22 V, with the lower-bias one having a small shoulder at 0.08 V above its position [Figure 3.12(a)]. All of these peaks have the same nodal pattern in the dI/dV maps as shown in Figure 3.12(b), which also compares the pattern to a DFT-simulation. If one end of the ribbon was contacted to the substrate using a voltage pulse from the STM tip detaching a hydrogen atom, the second peak at the intact end was found to decrease in magnitude.

The presence of two stronger peaks, separated by approximately 0.2 V, and their similar nodal patterns, raised the question whether the energy split of the zigzag-localized end states was observed in the experiment. The electronic states in finite 7-AGNRs were studied in more detail in Publication VIII. The theoretically predicted zigzag end states in the
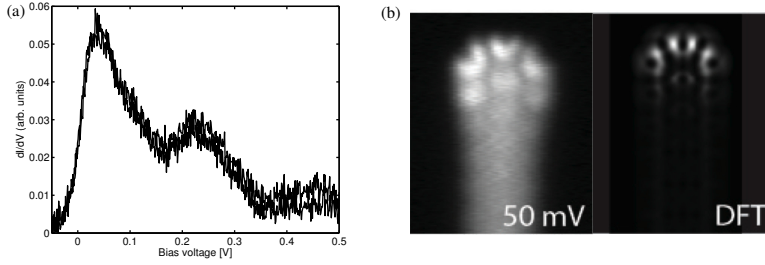
Figure 3.12. A comparison between experiment and theory on the dI/dV spectra of finite graphene nanoribbons (a) The STS spectrum measured at the zigzag end. (b) Left: The spatial dI/dV of the GNR end as imagined using a CO-terminated tip V = 0.05 V, Right: DFT simulation at E=0.1 eV. The background in the experimental image is due to inelastic tunneling processes.

uncharged finite ribbons consist of two pairs of energetically degenerate states that belong to different spin channels but are localized at the different ribbon termini. The pair lower in energy is occupied, leading to antiferromagnetically coupled ribbon termini, with the spin polarization as shown in Figure 3.13(a). The energy gap between the occupied and unoccupied states in the uncharged ribbons was calculated to be 0.43 eV using the PBE exchange-correlation functional [51] and it was not found to depend on the number of monomers in the ribbon [Figure 3.13(b), the inset]. Also a ferromagnetic coupling between the ribbon ends is possible. In the three-monomer ribbon, the antiferromagnetic state is only 1 meV lower in total energy, and this difference decreases with an increasing ribbon length. In a six-monomer ribbon, the difference is only 0.001 meV, corresponding to the temperature of merely 0.02 K. As the experimental ribbons, in general, are even longer, the ferromagnetic and antiferromagnetic states are likely to be practically degenerate.

The gaps between the end-localized states are greatly reduced if the ribbons are hole-doped. The doping is relevant in the experiment, as the end-state peak is on the positive bias, indicating that the mapped states are actually unoccupied. There are still two pairs of end-localized states but the degeneracy between the spin channels is broken, and a small split of the order of 1 meV is introduced between the two states of the same spin channel. The split between the end states of different spin species is approximately 0.22 eV in the ribbon doped by a single hole. Figure 3.13(b) shows the energy differences between the edge-localized states for no doping ($q = 0$) and hole-doped ($q = 1, 2$) ribbons as a function of the ribbon length.

Even though this split of 0.22 eV for $q = 1$ matches the experimentally observed separation, the corresponding intensities in the dI/dV spectra
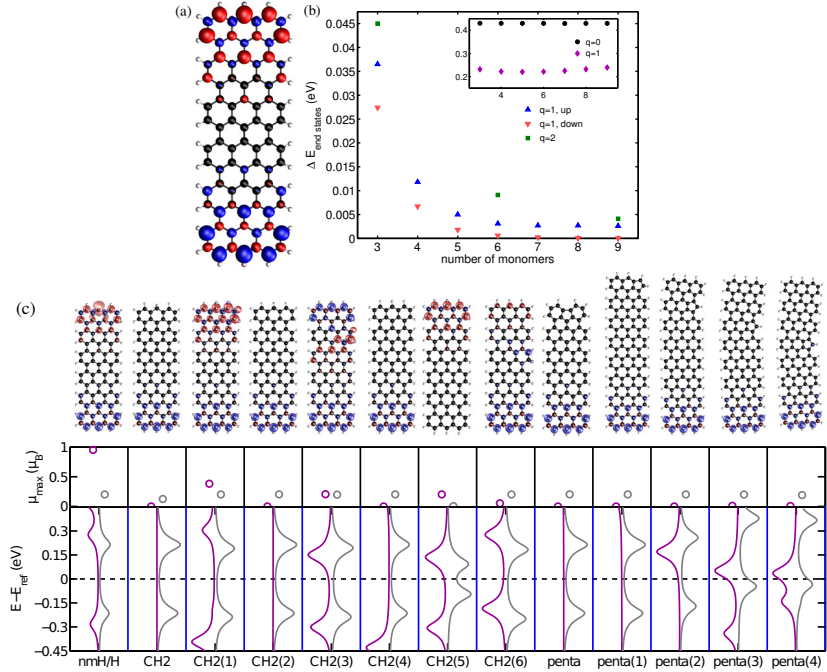
Figure 3.13. End-localized states in finite nanoribbons (a) The calculated spin density in an uncharged three-monomer ribbon. (b) The energy difference between the end-localized states in uncharged and hole-doped ribbons as a function of the ribbon length. Inset: uncharged ($q = 0$, black) ribbons with an antiferromagnetic ground state, energy difference between spin up- and spin down- end state pair for $q = 1$ (violet). Main figure: the energy splits between the end states in a single spin channel ($q = 1$, red and blue), the split between the end-localized states in each spin channel ($q = 2$, green). (c) The spin densities for an isosurface value of 0.01 Å (top row), the maximal spin moment at ribbon end (middle row) and the LDOS in the middle of the ribbon termini in the defected ribbons. Purple: defected end, gray: intact end. A description of the different defect types can be found in Publication VIII.
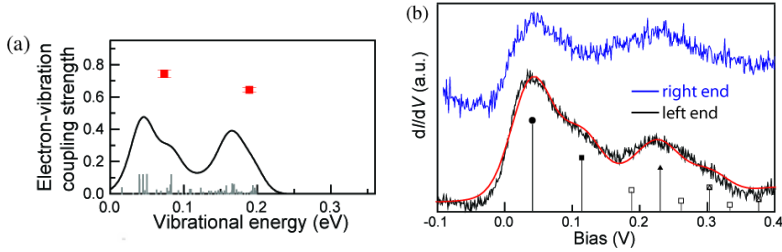
Figure 3.14. Inelastic tunneling in a three-monomer nanoribbon. (a) The calculated dimensionless electron-phonon coupling constants as a function of the phonon energy. Vertical gray lines: the calculated electron-phonon coupling, black line: Gaussian broadening of the calculated electron-phonon couplings with $\sigma = 0.015$ eV, $e^{-(E-\omega)^2/\sigma^2}$, red markers: the phonon energy and the electron-phonon coupling strength of the two-phonon model fitted to experiment. (b) Experimental dI/dV signal (black), as well as the transmission simulated from Eq. (3.7) by fitting two phonons to the experiment. Vertical lines with filled markers show the elastic peak as well as first-order replica and the open markers show the overtone and combination peak positions.

should also be similar if the two peaks were to result from two distinct electronic states. As vanilla DFT is known to underestimate the band gaps, the gap between the end states is likely to be larger in reality. For instance, in infinite zigzag nanoribbons, the use of a hybrid functional or the GW approximation more than doubles the spin-split gap [125, 126]. Moreover, as the experimental peak is fully on the positive bias side, all end states should be unoccupied corresponding thus to ribbon doping with two holes ($q = 2$). As Figure 3.13(b) shows, the $q = 2$ energy difference between the end-localized states does not match the experimental observation. Naturally, the substrate might screen electron-electron interactions and reduce gaps closer to their vanilla DFT values but, in any case, the presence of a shoulder at 0.08 V cannot be explained with end-localized electronic states.

To further exclude the spin-split end state as an explanation for the second peak, the energy level structure of end-localized states was studied in ribbons with a defect at one end. In the experiment, defecting one end lead to a decrease in the magnitude of the second dI/dV peak. Figure 3.13(c) illustrates the effect of the different defects on the spin polarization, the maximal spin moment at the carbon atoms, and on the LDOS at the ribbon ends. It is seen that at the intact end, the energy split between the end-localized states is roughly constant at 0.4 eV, and thus widely unperturbed by the defect. If the observed peaks were due to energy-split end-localized states, introducing a defect should not have much effect on the electronic structure at the intact end.

In Publication VII, an alternative explanation for the side peaks was

found. The energies of the side peak and shoulder match the graphene phonon energies well, ranging up to approximately 1600 cm^{-1} (0.2 eV). In vibronic tunneling, the transfer of an electron is accompanied by the emission or the absorption of a phonon. Consequently, phonon-induced peaks appear in the tunneling spectra, their positions and heights being determined by the phonon energy and the strength of the electron-phonon coupling. At a low temperature, the number of phonons is low, and thus emission processes are predominant. If only the emission process is allowed, the satellite peaks appear at positive bias with respect to the elastic peak. The observation of the phonon replicas is also dependent on the lifetime of the electronic state excited by the tunneling event. Consequently, vibronic replicas in STS experiments are usually observed in samples where the coupling between the molecule and the substrate is weak, for instance if a thin insulating layer is deposited between the metallic substrate and the molecule [127]. The presence of such replicas on the metal surface indicates that the coupling between graphene and the substrate indeed is weak. The decrease in the magnitude of the replicas after contacting the ribbon with the substrate corresponds to an increased coupling between the ribbon and the substrate, and, consequently, decreased lifetime of the tunneling electron on the ribbon.

In order to study this hypothesis, the vibrational frequencies of a three-monomer ribbon were calculated by solving the coupled perturbed Kohn-Sham equations as implemented in the density-functional theory package ADF [128]. The dimensionless electron-phonon coupling constants λ_β for all vibrational modes β were determined by calculating the Franck-Condon factors [129, 130]. The calculated dimensionless electron-phonon coupling constant as a function of the vibrational mode energy is shown in Figure 3.14(a).

The dI/dV signal in the presence of phonon replicas was simulated using the approach by Wingreen *et al.* [131, 132]. The zigzag end state was considered to be a single orbital with energy ϵ_0, and the STM tip and the substrate were treated as leads within the wide band approximation assuming a constant density of states in the leads in the relevant energy range. The transmission for incoming electrons with energy ϵ is then given by [131, 132]

$$T(\epsilon) \propto \int_{-\infty}^{\infty} \frac{d\sigma}{\hbar} e^{-\frac{\Gamma|\sigma|}{2\hbar} + \frac{i(\epsilon - \epsilon_0 + \lambda)}{\hbar} - \sum_\beta \left|\frac{M_\beta}{\hbar\omega_\beta}\right|^2 \left\{ (1 + 2N_{\omega_\beta})(1 - \cos(\omega_\beta\sigma)) + i\sin(\omega_\beta\sigma) \right\}},$$
$$(3.7)$$

where $\Gamma = (\Gamma_L + \Gamma_R)/2$ is the averaged elastic coupling to the leads L and R, $\lambda = \sum_\beta \left(M_\beta^2/\hbar\omega_\beta \right)$, and N_{ω_β} is the Bose-Einstein occupation factor.
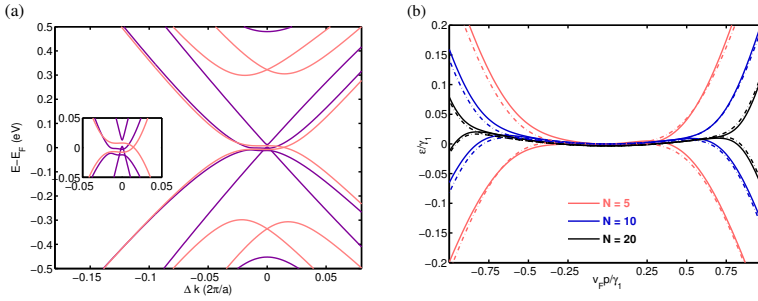
Figure 3.15. The band structure of multilayer graphene (a) The band structure close to the K-point ($\Delta k = 0$) for three-layer graphene slabs with Bernal (purple) and rhombohedral (red) stacking. The inset highlights the differences in the bands at very low energies. (b) The band structure of 5-, 10-, and 20-layer rhombohedral graphene stacks in the vicinity of the K point calculated with DFT (solid) and the fitted tight-binding model (dash-dotted).

Figure 3.14(b) shows the experimental measurement and the transmission curve simulated from Eq. (3.7), obtained by fitting two phonons and electron-phonon coupling coefficients. A comparison between the phonon energies and the electron-phonon coupling strengths calculated with DFT and the fitted values is shown in Figure 3.14(a). The fitted values, shown as red markers, agree well with the DFT calculation and the simulated dI/dV signal matches the experiment well. Thus, vibronic tunneling was found to explain both the peak positions and the intensities of the experimental dI/dV measurement.

3.3   Superconductivity in rhombohedral graphene slabs

In monolayer graphene, the electronic dispersion at the corners of the Brillouin zone is linear. In multilayers, the interaction between adjacent layers modifies the dispersion and, for instance, in bilayer graphene the dispersion becomes parabolic. Interestingly, in rhombohedral graphene stacks of N atom layers, a flat-band region appears in the vicinity of the K point [133, 134], and its width is dependent on the number of layers. Figure 3.15(a) compares the band structure trilayer graphene with Bernal and rhombohedral stacking, calculated using DFT. Figure 3.15(b) demonstrates how the width of the flat-band region increases with an increasing number of layers in rhombohedral graphene stacks.

The modern description of superconductivity is based on the Bardeen-Cooper-Schrieffer (BCS) theory [135]. The central idea of the theory is the formation of a two-electron bound state, called a Cooper pair, due to the presence of an attractive electron-electron interaction. This attraction
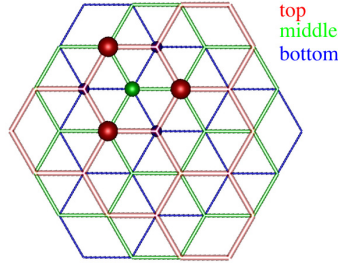
Figure 3.16. The top view of the stacking order in rhombohedral graphite. The red, green and blue bond networks illustrate the three displaced graphene layers. The sites connected by the γ_4 coupling from the middle layer, that is nearest-neighbor sites in adjacent layers belonging to the same sublattice, are indicated by opaque spheres.

can arise, for instance, from the coupling between electrons and phonons but, in general, its origin need not be known. Due to the Pauli exclusion principle, the Cooper pairs are correlated, and a gap emerges in the single-particle excitation spectrum in the superconducting state. The magnitude of the gap can be solved from the Bogoliubov-de Gennes equations that couple the electron and hole Hamiltonians by the superconducting order parameter Δ representing the superconducting gap. The band dispersion in the normal state is correlated with the magnitude of the superconducting coupling.

In addition to usual BCS-type bulk superconductivity, flat-band superconductivity with a rather high critical temperature for the superconducting transition has recently been suggested to arise in rhombohedral graphene stacks [136]. Moreover, this superconductivity type dominates over bulk superconductivity.

A simple nearest-neighbor tight-binding model was used in the analysis of Ref. [136]. The effect of couplings to neighbors farther away on the superconducting state was addressed in Publication IX. In addition to the flat-band mechanism, also BCS-type surface superconductivity was found to be relevant. In order to address the crossover between these two, an accurate tight-binding model able to accurately describe the band structure close to the K points was needed. In the literature, different tight-binding parameter sets have been reported for rhombohedral graphene stacks or graphite [7, 37]. Especially the magnitude of the non-perpendicular out-of-plane hopping amplitude, γ_4 [see Figure 3.16], is not unambiguous and varies by an order of magnitude. Moreover, the tight-binding fits usually try to capture the overall band structure, whereas in this case, a description of the flat band region, as accurate as possible was required.

The band structures for rhombohedral graphene slabs consisting of five
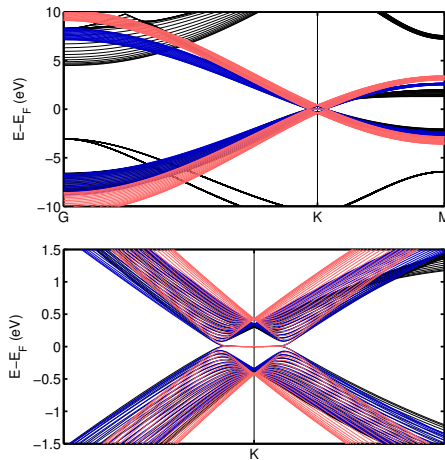
Figure 3.17. The fit of the tight-binding model to the DFT band structure of a 20-layer ABC-stacked slab. Black: DFT band structure, red and blue: the two different sets of tight-binding parameters with similar agreement close to the K point. Top: the band structure along the Γ-K-M direction in the Brillouin zone, Bottom: a close-up from the vicinity of the K point [see Figure 3.15(b) for further magnification].

to twenty layers were calculated using the density-functional theory. The tight-binding model with nearest-neighbor in-plane coupling as well as the out-of-plane couplings, as specified in Figures 2.2 and 3.16, was fitted to the bands closest to the Fermi energy with a weak parabolic dispersion in the vicinity of the K point. Two fits showing similar agreement close to the K point were found, and the corresponding band structures are shown in Figure 3.17. The flat-band region close to the K-point is better illustrated in Figure 3.15(b), in which the solid lines show the DFT calculation and dash-dotted lines the tight-binding fit. As one of the parameter sets better captures the overall band structure, with the tight-binding parameter values γ_0 = 2.58 eV, γ_1 = 0.34 eV, γ_3= 0.17 eV, and γ_4= 0.04 eV, it was chosen for further calculations characterizing the superconducting state. It is worth noting that both fits give similar values for derived quantities, such as the effective electron mass in the parabolic band and the parameter α used to characterize the energy scale relevant to the superconducting transition in Publication IX.

4. Summary

In this thesis, the electronic properties of chemically modified and nanostructured graphene systems were addressed using density-functional theory and lattice models. Additionally, Publication I introduces the lattice density functional theory method for graphene, which improves over the widely-used mean-field approximation of the Hubbard model.

Publication II, Publication III, Publication IV and Publication V address using density-functional theory the chemical interactions between graphene or carbon nanotubes, and hydrogen and chlorine used to functionalize them. For a realistic description, the gaseous environment containing the functionalizing species is considered using *ab initio* thermodynamics. In the case of graphene, also the effect of a widely used insulating substrate, SiO_2 on the functionalization is studied.

Publication VI, Publication VII and Publication VIII address the electronic properties of metal-deposited finite graphene nanostructures and compare the calculations with experimental scanning tunneling spectroscopy measurements. Collective states arising from a large number of molecular orbitals observed as confined states in scanning tunneling spectroscopy, electron-phonon coupling in finite graphene nanoribbons, as well as the effect of structural imperfections and doping on the theoretically predicted electronic states localized at the zigzag ends is addressed using both the tight-binding model and density-functional theory.

Publication IX studies the prospects of superconductivity in rhombohedral graphite surfaces. The parameters of a tight-binding model capable of accurately describing the flat-band region close to the K point at the corner of the Brillouin zone are determined from density-functional theory calculations.

Bibliography

[1] H. W. Kroto, J. R. Heath, S. C. O'Brien, R. F. Curl, and R. E. Smalley, "C_{60}: Buckminsterfullerene," *Nature*, vol. 318, p. 162, 1985.

[2] S. Iijima, "Helical microtubules of graphitic carbon," *Nature*, vol. 354, p. 56, 1991.

[3] P. R. Wallace, "The band theory of graphite," *Phys. Rev.*, vol. 71, p. 622, 1947.

[4] K. S. Novoselov, A. K. Geim, S. V. Morozov, D. Jiang, Y. Zhang, S. V. Dubonos, I. V. Grigorieva, and A. A. Firsov, "Electric field effect in atomically thin carbon films," *Science*, vol. 306, p. 666, 2004.

[5] A. J. van Bommel, J. E. Crombeen, and A. van Tooren, "LEED and Auser electron observations of the SiC(0001) surface," *Surf. Sci.*, vol. 48, p. 463, 1975.

[6] A. E. Karu and M. Beer, "Pyrolytic formation of highly crystalline graphite films," *J. Appl Phys.*, vol. 37, p. 2179, 1966.

[7] A. H. Castro Neto, F. Guinea, N. M. R. Peres, K. S. Novoselov, and A. K. Geim, "The electronic properties of graphene," *Rev. Mod. Phys.*, vol. 81, p. 109, 2009.

[8] K. Nakada, M. Fujita, G. Dresselhaus, and M. S. Dresselhaus, "Edge state in graphene ribbons: Nanometer size effect and edge shape dependence," *Phys. Rev. B*, vol. 54, p. 17954, 1996.

[9] H. Lee, Y.-W. Son, N. Park, S. Han, and J. Yu, "Magnetic ordering at the edges of graphitic fragments: Magnetic tail interactions between the edge-localized states," *Phys. Rev. B*, vol. 72, p. 174431, 2005.

[10] M. Y. Han, B. Özyilmaz, Y. Zhang, and P. Kim, "Energy band-gap engineering of graphene nanoribbons," *Phys. Rev. Lett.*, vol. 98, p. 206805, 2007.

[11] W. L. Wang, S. Meng, and E. Kaxiras, "Graphene nanoflakes with large spin," *Nano Lett.*, vol. 8, p. 241, 2008.

[12] W. L. Wang, O. V. Yazyev, S. Meng, and E. Kaxiras, "Topological frustration in graphene nanoflakes: Magnetic order and spin logic devices," *Phys. Rev. Lett.*, vol. 102, p. 157201, 2009.

[13] J.-U. Park, S.-W. Nam, M.-S. Lee, and C. M. Lieber, "Synthesis of monolithic graphene–graphite integrated electronics," *Nature Mater.*, vol. 11, p. 120, 2011.

[14] Y.-M. Lin, C. Dimitrakopoulos, K. A. Jenkins, D. B. Farmer, H.-Y. Chiu, A. Grill, and P. Avouris, "100-GHz transistors from wafer-scale epitaxial graphene," *Science*, vol. 327, p. 662, 2010.

[15] F. Bonaccorso, Z. Sun, T. Hasan, and A. C. Ferrari, "Graphene photonics and optoelectronics," *Nature Phot.*, vol. 4, p. 611, 2010.

[16] Z. Sun, T. Hasan, F. Torrisi, D. Popa, G. Privitera, F. Wang, F. Bonaccorso, D. M. Basko, and A. C. Ferrari, "Graphene mode-locked ultrafast laser," *ACS Nano*, vol. 4, p. 803, 2010.

[17] F. Xia, T. Mueller, Y.-M. Lin, A. Valdes-Garcia, and P. Avouris, "Ultrafast graphene photodetector," *Nature Nanotech.*, vol. 4, p. 839, 2009.

[18] F. Schedin, A. K. Geim, S. V. Morozov, E. W. Hill, P. Blake, M. I. Katsnelson, and K. S. Novoselov, "Detection of individual gas molecules adsorbed on graphene," *Nature Mater.*, vol. 6, p. 652, 2007.

[19] D. Cohen-Tanugi and J. C. Grossman, "Water desalination across nanoporous graphene," *Nano Lett.*, vol. 12, p. 3602, 2012.

[20] S. Bae, H. Kim, Y. Lee, X. Xu, J.-S. Park, Y. Zheng, J. Balakrishnan, T. Lei, H. R. Kim, Y. I. Song, Y.-J. Kim, K. S. Kim, B. Özyilmaz, J.-H. Ahn, B. H. Hong, and S. Iijima, "Roll-to-roll production of 30-inch graphene films for transparent electrodes," *Nature Nanotech.*, vol. 5, p. 574, 2010.

[21] M. Olle, G. Ceballos, D. Serrate, and P. Gambardella, "Yield and shape selection of graphene nanoislands grown on Ni(111)," *Nano Lett.*, vol. 12, p. 4431, 2012.

[22] A. K. Geim and K. S. Novoselov, "The rise of graphene," *Nature Mat.*, vol. 6, p. 183, 2007.

[23] J. Cai, P. Ruffieux, R. Jaafar, M. Bieri, T. Braun, S. Blankenburg, M. Muoth, A. P. Seitsonen, M. Saleh, X. Feng, K. Müllen, and R. Fasel, "Atomically precise bottom-up fabrication of graphene nanoribbons," *Nature*, vol. 466, p. 470, 2010.

[24] M. Treier, C. A. Pignedoli, T. Laino, R. Rieger, K. Müllen, D. Passerone, and R. Fasel, "Surface-assisted cyclodehydrogenation provides a synthetic route towards easily processable and chemically tailored nanographenes," *Nature Chem.*, vol. 3, p. 61, 2011.

[25] K. V. Emtsev, A. Bostwick, K. Horn, J. Jobst, G. L. Kellogg, L. Ley, J. L. McChesney, T. Ohta, S. A. Reshanov, J. Röhrl, E. Rotenberg, A. K. Schmid, D. Waldmann, H. B. Weber, and T. Seyller, "Towards wafer-size graphene layers by atmospheric pressure graphitization of silicon carbide," *Nature Materials*, vol. 8, p. 203, 2009.

[26] D. V. Kosynkin, A. L. Higginbotham, A. Sinitskii, J. R. Lomeda, A. Dimiev, B. K. Price, and J. M. Tour, "Longitudinal unzipping of carbon nanotubes to form graphene nanoribbons," *Nature*, vol. 458, p. 872, 2009.

[27] D. C. Elias, R. V. Gorbachev, A. S. Mayorov, S. V. Morozov, A. A. Zhukov, P. Blake, L. A. Ponomarenko, I. V. Grigorieva, K. S. Novoselov, F. Guinea, and A. K. Geim, "Dirac cones reshaped by interaction effects in suspended graphene," *Nature Phys.*, vol. 7, p. 701, 2011.

[28] J. Martin, N. Akerman, G. Ulbricht, T. Lohmann, J. H. Smet, K. von Klitzing, and A. Yacoby, "Observation of electron-hole puddles in graphene using a scanning single-electron transistor," *Nature Phys.*, vol. 4, p. 144, 2008.

[29] C. R. Dean, A. F. Young, I. Meric, C. Lee, L. Wang, S. Sorgenfrei, K. Watanabe, T. Taniguchi, P. Kim, K. L. Shepard, and J. Hone, "Boron nitride substrates for high-quality graphene electronics," *Nature Nanotech.*, vol. 5, p. 722, 2010.

[30] D. C. Elias, R. R. Nair, T. M. G. Mohiuddin, S. V. Morozov, P. Blake, M. P. Halsall, A. C. Ferrari, D. W. Bouhkvalov, M. I. Katsnelson, A. K. Geim, and K. S. Novoselov, "Control of graphene's properties by reversible hydrogenation: Evidence for graphane," *Science*, vol. 323, p. 610, 2009.

[31] R. Zbořil, F. Karlický, A. B. Bourlinos, T. A. Steriotis, A. K. Stubos, V. Georgakilas, K. Šafáařová, D. Jančík, C. Trapalis, and M. Otyepka, "Graphene fluoride: A stable stoichiometric graphene derivative and its chemical conversion to graphene," *Small*, vol. 6, p. 2885, 2010.

[32] R. R. Nair, W. Ren, R. Jalil, I. Riaz, V. G. Kravets, L. Britnell, P. Blake, F. Schedin, A. S. Mayorov, S. Yuan, M. I. Katsnelson, H.-M. Cheng, W. Strupinski, L. G. Bulusheva, A. V. Okotrub, I. V. Grigorieva, A. N. Grigorenko, K. S. Novoselov, and A. K. Geim, "Fluorographene: A two-dimensional counterpart of Teflon," *Small*, vol. 6, p. 2877, 2010.

[33] R. Lv, Q. Li, Andrés, R. Botello-Méndez, T. Hayashi, B. Wang, A. Berkdemir, Q. Hao, A. L. Elías, R. Cruz-Silva, H. R. Gutiérrez, Y. A. Kim, H. Muramatsu, J. Zhu, M. Endo, H. Terrones, J.-C. Charlier, M. Pan, and M. Terrones, "Nitrogen-doped graphene: beyond single substitution and enhanced molecular sensing," *Sci. Rep.*, vol. 2, p. 586, 2012.

[34] Y. A. Kim, K. Fujisawa, H. Muramatsu, T. Hayashi, M. Endo, T. Fujimori, K. Kaneko, M. Terrones, J. Behrends, A. Eckmann, C. Casiraghi, K. S. Novoselov, R. Saito, and M. S. Dresselhaus, "Raman spectroscopy of boron-doped single-layer graphene," *ACS Nano*, vol. 6, p. 6293, 2012.

[35] K. F. Mak, C. H. Lui, J. Shan, and T. F. Heinz, "Observation of an electric-field-induced band gap in bilayer graphene by infrared spectroscopy," *Phys. Rev. Lett.*, vol. 102, p. 256405, 2009.

[36] J. J. Hubbard, "Electron correlations in narrow energy bands," *Proc. Royal Soc. Lond. A*, vol. 276, p. 238, 1963.

[37] J. McClure, "Electron energy band structure and electronic properties of rhombohedral graphite," *Carbon*, vol. 7, p. 425, 1969.

[38] Y. Hancock, A. Uppstu, K. Saloriutta, A. Harju, and M. J. Puska, "Generalized tight-binding transport model for graphene nanoribbon-based systems," *Phys. Rev. B*, vol. 81, p. 245402, 2010.

[39] P. Gava, M. Lazzeri, A. M. Saitta, and F. Mauri, "Ab initio study of gap opening and screening effects in gated bilayer graphene," *Phys. Rev. B*, vol. 79, p. 165431, 2009.

[40] L. M. Malard, J. Nilsson, D. C. Elias, J. C. Brant, F. Plentz, E. S. Alves, A. H. Castro Neto, and M. A. Pimenta, "Probing the electronic structure of bilayer graphene by Raman scattering," *Phys. Rev. B*, vol. 76, p. 201401, 2007.

[41] J. Hicks, M. Sprinkle, K. Shepperd, F. Wang, A. Tejeda, A. Taleb-Ibrahimi, F. Bertran, P. L. Fèvre, W. A. de Heer, C. Berger, and E. H. Conrad, "Symmetry breaking in commensurate graphene rotational stacking: Comparison of theory and experiment," *Phys. Rev. B*, vol. 83, p. 205403, 2011.

[42] A. Luican, G. Li, A. Reina, J. Kong, R. R. Nair, K. S. Novoselov, A. K. Geim, and E. Y. Andrei, "Single-layer behavior and its breakdown in twisted graphene layers," *Phys. Rev. Lett.*, vol. 106, p. 126802, 2011.

[43] J. C. Slonczewski and P. R. Weiss, "Band structure of graphite," *Phys. Rev.*, vol. 109, p. 272, 1958.

[44] A. D. Güçlü, P. Potasz, O. Voznyy, M. Korkusinski, and P. Hawrylak, "Magnetism and correlations in fractionally filled degenerate shells of graphene quantum dots," *Phys. Rev. Lett.*, vol. 103, p. 246805, 2009.

[45] V. N. Kotov, B. Uchoa, V. M. Pereira, F. Guinea, and A. H. Castro Neto, "Electron-electron interactions in graphene: Current status and perspectives," *Rev. Mod. Phys.*, vol. 84, p. 1067, 2012.

[46] Y.-W. Son, M. L. Cohen, and S. G. Louie, "Half-metallic graphene nanoribbons," *Nature*, vol. 444, p. 347, 2006.

[47] G. Lanczos, "An iteration for the solution of the eigenvalue problem of linear differential and integral operators," *J. Res. Nat. Bur. Standards*, vol. 45, p. 255, 1950.

[48] J. M. Thijssen, *Computational Physics*. Cambridge University Press, 1st ed., 1999.

[49] P. Hohenberg and W. Kohn, "Inhomogeneous electron gas," *Phys. Rev.*, vol. 136, p. B864, 1964.

[50] W. Kohn and L. J. Sham, "Self-consistent equations including exchange and correlation effects," *Phys. Rev.*, vol. 140, p. A1133, 1965.

[51] J. P. Perdew, K. Burke, and M. Ernzerhof, "Generalized gradient approximation made simple," *Phys. Rev. Lett.*, vol. 77, p. 3865, 1996.

[52] K. Burke, "Perspective on density functional theory," *J. Chem. Phys.*, vol. 136, p. 150901, 2012.

[53] V. Blum, R. Gehrke, F. Hanke, P. Havu, V. Havu, X. Ren, K. Reuter, and M. Scheffler, "Ab initio molecular simulations with numeric atom-centered orbitals," *Comp. Phys. Comm.*, vol. 180, p. 2175, 2009.

[54] J. P. Perdew, R. G. Parr, M. Levy, and J. L. Balduz, Jr. , "Density-functional theory for fractional particle number: Derivative discontinuities of the energy," *Phys. Rev. Lett.*, vol. 49, p. 1691, 1982.

[55] F. Aryasetiawan and O. Gunnarsson, "The GW method," *Rep. Prog. Phys.*, vol. 61, p. 237, 1998.

[56] E. Runge and E. K. U. Gross, "Density-functional theory for time-dependent systems," *Phys. Rev. Lett.*, vol. 52, p. 997, 1984.

[57] H. A. Bethe and E. E. Salpeter, "A relativistic equation for bound state problems," *Phys. Rev.*, vol. 82, p. 309, 1951.

[58] K. Schönhammer and O. Gunnarsson, "Discontinuity of the exchange potential in density functional theory," *J. Phys. C*, vol. 20, p. 3675, 1987.

[59] G. Xianlong, A.-H. Chen, I. V. Tokatly, and S. Kurth, "Lattice density functional theory at finite temperature with strongly density-dependent exchange-correlation potentials," *Phys. Rev. B*, vol. 86, p. 235139, 2012.

[60] A. Schindlmayr and R. W. Godby, "Density-functional theory and the v-representability problem for model strongly correlated electron systems," *Phys. Rev. B*, vol. 51, p. 10427, 1995.

[61] W. Kohn, "v-representability and density functional theory," *Phys. Rev. Lett.*, vol. 51, p. 1596, 1983.

[62] K. Capelle, N. A. Lima, M. F. Silva, and L. N. Oliveira, "Density-functional theory for the Hubbard model: numerical results for the Luttinger liquid and the Mott insulator," in *The Fundamentals of Electron Density, Density Matrix and Density-Functional Theory in Atoms, Molecules and the Solid State*, pp. 145–168, Kluwer Academic Publishers, Netherlands, 2003.

[63] E. H. Lieb, "Two theorems on the Hubbard model," *Phys. Rev. Lett.*, vol. 62, p. 1201, 1989.

[64] J. Rogal, *Stability, composition and function of palladium surfaces in oxidizing environments: A first-principles statistical mechanics approach*. PhD thesis, Freie Universität Berlin, 2006.

[65] T. Wassmann, A. P. Seitsonen, A. M. Saitta, M. Lazzeri, and F. Mauri, "Structure, stability, edge states, and aromaticity of graphene ribbons," *Phys. Rev. Lett.*, vol. 101, p. 096402, 2008.

[66] M. W. Chase, Jr, C. A. Davies, J. R. Downey, Jr., D. J. Frurip, R. A. McDonald, and A. N. Syverud, "JANAF Thermochemical Tables Third Edition," *J. Phys. Chem. Ref. Data*, vol. 14, Suppl. 1, p. 927, 1985.

[67] T. P. M. Goumans, A. Wander, W. A. Brown, and C. R. A. Catlow, "Structure and stability of the (001) α-quartz surface," *Phys. Chem. Chem. Phys.*, vol. 9, p. 2146, 2007.

[68] J. O. Sofo, A. S. Chaudhari, and G. D. Barber, "Graphane: A two-dimensional hydrocarbon," *Phys. Rev. B*, vol. 75, p. 153401, 2007.

[69] A. K. Singh and B. I. Yakobson, "Electronics and magnetism of patterned graphene nanoroads," *Nano Lett.*, vol. 9, p. 1540, 2009.

[70] R. Balog, B. Jørgensen, L. Nilsson, M. Andersen, E. Rienks, M. Bianchi, M. Fanetti, E. Lægsgaard, A. Baraldi, S. Lizzit, Z. Sljivancanin, F. Besenbacher, B. Hammer, T. G. Pedersen, P. Hofmann, and L. Hornekær, "Bandgap opening in graphene induced by patterned hydrogen adsorption," *Nature Mat.*, vol. 9, p. 315, 2010.

[71] D. Haberer, D. V. Vyalikh, S. Taioli, B. Dora, M. Farjam, J. Fink, D. Marchenko, T. Pichler, K. Ziegler, S. Simonucci, M. S. Dresselhaus, M. Knupfer, B. Bücher, and A. Grüneis, "Tunable band gap in hydrogenated quasi-free-standing graphene," *Nano Lett.*, vol. 10, p. 3360, 2010.

[72] S. Ryu, M. Y. Han, J. Maultzsch, T. F. Heiz, P. Kim, M. L. Steigerwald, and L. E. Brus, "Reversible basal plane hydrogenation of graphene," *Nano Lett.*, vol. 8, p. 4597, 2008.

[73] P. Sessi, J. R. Guest, M. Bode, and N. P. Guisinger, "Patterning graphene at the nanometer scale via hydrogen desorption," *Nano Lett.*, vol. 9, p. 4343, 2009.

[74] N. P. Guisinger, G. M. Rutter, J. N. Crain, P. N. First, and J. A. Stroscio, "Exposure of epitaxial graphene on SiC(0001) to atomic hydrogen," *Nano Lett.*, vol. 9, p. 1462, 2009.

[75] R. Balog, B. Jørgensen, J. Wells, E. Lægsgaard, P. Hofmann, F. Besenbacher, and L. Hornekær, "Atomic hydrogen adsorbate structures on graphene," *J. Am. Chem. Soc.*, vol. 131, p. 8744, 2009.

[76] M. Andersen, L. Hornekær, and B. Hammer, "Graphene on metal surfaces and its hydrogen adsorption: A meta-GGA functional study," *Phys. Rev. B*, vol. 86, p. 085405, 2012.

[77] H. J. Xiang, E. J. Kan, S.-H. Wei, X. G. Gong, and M.-H. Whangbo, "Thermodynamically stable single-side hydrogenated graphene," *Phys. Rev. B*, vol. 82, p. 165425, 2010.

[78] A. Tkatchenko and M. Scheffler, "Accurate molecular van der Waals interactions from ground-state electron density and free-atom reference data," *Phys. Rev. Lett.*, vol. 102, p. 073005, 2009.

[79] J. T. Robinson, J. S. Burgess, C. E. Junkermeier, S. C. Badescu, T. L. Reinecke, F. K. Perkins, M. K. Zalalutdniov, J. W. Baldwin, J. C. Culbertson, P. E. Sheehan, and E. S. Snow, "Properties of fluorinated graphene films," *Nano Lett.*, vol. 10, p. 3001, 2010.

[80] O. Leenaerts, H. Peelaers, A. D. Hernández-Nieves, B. Partoens, and F. M. Peeters, "First-principles investigation of graphene fluoride and graphane," *Phys. Rev. B*, vol. 82, p. 195436, 2010.

[81] M. Klintenberg, S. Lèbegue, M. I. Katsnelson, and O. Eriksson, "Theoretical analysis of the chemical bonding and electronic structure of graphene interacting with group IA and group VIIA elements," *Phys. Rev. B*, vol. 81, p. 085433, 2010.

[82] B. Li, L. Zhou, D. Wu, H. Peng, K. Yan, Y. Zhou, and Z. Liu, "Photochemical chlorination of graphene," *ACS Nano*, vol. 5, p. 5957, 2011.

[83] P. V. C. Medeiros, A. J. S. Mascarenhas, F. de Brito Mota, and C. M. C. de Castilho, "A DFT study of halogen atoms adsorbed on graphene layers," *Nanotechnology*, vol. 21, p. 485701, 2010.

[84] T. O. Wehling, M. I. Katsnelson, and A. I. Lichtenstein, "Impurities on graphene: Midgap states and migration barriers," *Phys. Rev. B*, vol. 80, p. 085428, 2009.

[85] Y. G. Zhou, X. T. Zu, F. Gao, H. F. Lv, and H. Y. Xiao, "Adsorption-induced magnetic properties and metallic behavior of graphene," *Appl. Phys. Lett.*, vol. 95, p. 123119, 2009.

[86] A. N. Rudenko, F. J. Keil, M. I. Katsnelson, and A. I. Lichtenstein, "Adsorption of diatomic halogen molecules on graphene: A van der Waals density functional study," *Phys. Rev. B*, vol. 82, p. 035427, 2010.

[87] H. Şahin and S. Ciraci, "Chlorine adsorption on graphene: Chlorographene," *J. Phys. Chem. C*, vol. 116, p. 24075, 2012.

[88] M. Yang, L. Zhou, J. Wang, Z. Liu, and Z. Liu, "Evolutionary chlorination of graphene: From charge-transfer complex to covalent bonding and nonbonding," *J. Phys. Chem. C*, vol. 116, p. 844, 2012.

[89] J. Wu, L. Xie, Y. Li, H. Wang, Y. Ouyang, J. Guo, and H. Dai, "Controlled chlorine plasma reaction for noninvasive graphene doping," *J. Am. Chem. Soc.*, vol. 133, p. 19668, 2011.

[90] L. Tsetseris and S. T. Pantelides, "Graphene nano-ribbon formation through hydrogen-induced unzipping of carbon nanotubes," *Appl. Phys. Lett.*, vol. 99, p. 143119, 2011.

[91] M. Wu, J. S. Tse, and J. Z. Jiang, "Unzipping of graphene by fluorination," *Phys. Chem. Lett.*, vol. 1, p. 1394, 2010.

[92] G. Lu, H. Scudder, and N. Kioussis, "Hydrogen-induced unzipping of single-walled carbon nanotubes," *Phys. Rev. B*, vol. 68, p. 205416, 2003.

[93] A. V. Talyzin, S. Luzan, I. V. Anoshkin, A. G. Nasibulin, H. Jiang, E. I. Kauppinen, V. M. Mikoushkin, V. V. Shnitov, D. E. Marchenko, and D. Noréus, "Hydrogenation, purification, and unzipping of carbon nanotubes by reaction with molecular hydrogen: Road to graphane nanoribbons," *ACS Nano*, vol. 5, p. 5132, 2011.

[94] L. Valentini, "Formation of unzipped carbon nanotubes by CF$_4$ plasma treatment," *Diam. Rel. Mat.*, vol. 20, p. 445, 2011.

[95] G. Giovannetti, P. A. Khomyakov, G. Brocks, V. M. Karpan, J. van den Brink, and P. J. Kelly, "Doping graphene with metal contacts," *Phys. Rev. Lett.*, vol. 101, p. 026803, 2008.

[96] P. A. Khomyakov, G. Giovannetti, P. C. Rusu, G. Brocks, J. van den Brink, and P. J. Kelly, "First-principles study of the interaction and charge transfer between graphene and metals," *Phys. Rev. B*, vol. 79, p. 195425, 2009.

[97] T. Olsen and K. S. Thygesen, "Random phase approximation applied to solids, molecules, and graphene-metal interfaces: From van der Waals to covalent bonding," *Phys. Rev. B*, vol. 87, p. 075111, 2013.

[98] I. Hamada and M. Otani, "Comparative van der Waals density-functional study of graphene on metal surfaces," *Phys. Rev. B*, vol. 82, p. 153412, 2010.

[99] J. Sławińska, P. Dabrowski, and I. Zasada, "Doping of graphene by a Au(111) substrate: Calculation strategy within the local density approximation and a semiempirical van der Waals approach," *Phys. Rev. B*, vol. 83, p. 245429, 2011.

[100] M. Vanin, J. J. Mortensen, A. K. Kelkkanen, J. M. Garcia-Lastra, K. S. Thygesen, and K. W. Jacobsen, "Graphene on metals: A van der Waals density functional study," *Phys. Rev. B*, vol. 81, p. 081408, 2010.

[101] D. Stradi, S. Barja, C. Díaz, M. Garnica, B. Borca, J. J. Hinarejos, D. Sánchez-Portal, M. Alcamí, A. Arnau, A. L. Vázquez de Parga, R. Miranda, and F. Martín, "Electron localization in epitaxial graphene on Ru(0001) determined by Moiré corrugation," *Phys. Rev. B*, vol. 85, p. 121404, 2012.

[102] C. Busse, P. Lazić, R. Djemour, J. Coraux, T. Gerber, N. Atodiresei, V. Caciuc, R. Brako, A. T. N'Diaye, S. Blügel, J. Zegenhagen, and T. Michely, "Graphene on Ir(111): Physisorption with chemical modulation," *Phys. Rev. Lett.*, vol. 107, p. 036101, 2011.

[103] S. Nie, N. C. Bartelt, J. M. Wofford, O. D. Dubon, K. F. McCarty, and K. Thürmer, "Scanning tunneling microscopy study of graphene on Au(111): Growth mechanisms and substrate interactions," *Phys. Rev. B*, vol. 85, p. 205406, 2012.

[104] E. N. Voloshina, E. Fertitta, A. Garhofer, F. Mittendorfer, M. Fonin, A. Thissen, and Y. S. Dedkov, "Electronic structure and imaging contrast of graphene Moiré on metals," *Sci. Rep.*, vol. 3, p. 1072, 2013.

[105] M. P. Boneschanscher, J. van der Lit, Z. Sun, I. Swart, P. Liljeroth, and D. Vanmaekelbergh, "Quantitative atomic resolution force imaging on epitaxial graphene with reactive and nonreactive AFM probes," *ACS Nano*, vol. 6, p. 10216, 2012.

[106] J. Tersoff and D. R. Hamann, "Theory and application for the scanning tunneling microscope," *Phys. Rev. Lett.*, vol. 50, p. 1998, 1983.

[107] J. Repp, G. Meyer, S. M. Stojković, A. Gourdon, and C. Joachim, "Molecules on insulating films: Scanning-tunneling microscopy imaging of individual molecular orbitals," *Phys. Rev. Lett.*, vol. 94, p. 026803, 2005.

[108] A. A. Radzig and B. Smirnov, *Reference Data on Atoms, Molecules, and Ions*. Springer Series in Chemical Physics 31, Springer-Verlag Berlin-Heidelberg, 1985.

[109] L. Gross, N. Moll, F. Mohn, A. Curioni, G. Meyer, F. Hanke, and M. Persson, "High-resolution molecular orbital imaging using a p-wave STM tip," *Phys. Rev. Lett.*, vol. 107, p. 086101, 2011.

[110] C. J. Chen, "Tunneling matrix elements in three-dimensional space: The derivative rule and the sum rule," *Phys. Rev. B*, vol. 42, p. 8841, 1990.

[111] D. Subramaniam, F. Libisch, Y. Li, C. Pauly, V. Geringer, R. Reiter, T. Mashoff, M. Liebmann, J. Burgdörfer, C. Busse, T. Michely, R. Mazzarello, M. Pratzer, and M. Morgenstern, "Wave-function mapping of graphene quantum dots with soft confinement," *Phys. Rev. Lett.*, vol. 108, p. 046801, 2012.

[112] I. Pletikosić, M. Kralj, P. Pervan, R. Brako, J. Coraux, A. T. N'Diaye, C. Busse, and T. Michely, "Dirac cones and minigaps for graphene on Ir(111)," *Phys. Rev. Lett.*, vol. 102, p. 056808, 2009.

[113] S. Rusponi, M. Papagno, P. Moras, S. Vlaic, M. Etzkorn, P. M. Sheverdyaeva, D. Pacilé, H. Brune, and C. Carbone, "Highly anisotropic Dirac cones in epitaxial graphene modulated by an island superlattice," *Phys. Rev. Lett.*, vol. 105, p. 246803, 2010.

[114] E. Starodub, A. Bostwick, L. Moreschini, S. Nie, F. El Gabaly, K. F. McCarty, and E. Rotenberg, "In-plane orientation effects on the electronic structure, stability, and Raman scattering of monolayer graphene on Ir(111)," *Phys. Rev. B*, vol. 83, p. 125428, 2011.

[115] S.-H. Phark, J. Borme, A. L. Vanegas, M. Corbetta, D. Sander, and J. Kirschner, "Direct observation of electron confinement in epitaxial graphene nanoislands," *ACS Nano*, vol. 5, p. 8162, 2011.

[116] S. J. Altenburg, J. Kröger, T. O. Wehling, B. Sachs, A. I. Lichtenstein, and R. Berndt, "Local gating of an Ir(111) surface resonance by graphene islands," *Phys. Rev. Lett.*, vol. 108, p. 206805, 2012.

[117] H. Huang, D. Wei, J. Sun, S. L. Wong, Y. P. Feng, A. H. Castro Neto, and A. T. S. Wee, "Spatially resolved electronic structures of atomically precise armchair graphene nanoribbons," *Sci. Rep.*, vol. 2, p. 983, 2012.

[118] S. Linden, D. Zhong, A. Timmer, N. Aghdassi, J. H. Franke, H. Zhang, X. Feng, K. Müllen, H. Fuchs, L. Chi, and H. Zacharias, "Electronic structure of spatially aligned graphene nanoribbons on Au(788)," *Phys. Rev. Lett.*, vol. 108, p. 216801, 2012.

[119] P. Ruffieux, J. Cai, N. C. Plumb, L. Patthey, D. Prezzi, A. Ferretti, E. Molinari, X. Feng, K. Müllen, C. A. Pignedoli, and R. Fasel, "Electronic structure of atomically precise graphene nanoribbons," *ACS Nano*, vol. 6, p. 6930, 2012.

[120] L. Talirz, H. Söde, J. Cai, P. Ruffieux, S. Blankenburg, R. Jafaar, R. Berger, X. Feng, K. Müllen, D. Passerone, R. Fasel, and C. A. Pignedoli, "Termini of bottom-up fabricated graphene nanoribbons," *J. Am. Chem. Soc.*, vol. 135, p. 2060, 2013.

[121] M. Koch, F. Ample, C. Joachim, and L. Grill, "Voltage-dependent conductance of a single graphene nanoribbon," *Nature Nanotech.*, vol. 7, p. 713, 2012.

[122] C. Bronner, F. Leyssner, S. Stremlau, M. Utecht, P. Saalfrank, T. Klamroth, and P. Tegeder, "Electronic structure of a subnanometer wide bottom-up fabricated graphene nanoribbon: End states, band gap, and dispersion," *Phys. Rev. B*, vol. 86, p. 085444, 2012.

[123] S. Blankenburg, J. Cai, P. Ruffieux, R. Jaafar, D. Passerone, X. Feng, K. Müllen, R. Fasel, and C. A. Pignedoli, "Intraribbon heterojunction formation in ultranarrow graphene nanoribbons," *ACS Nano*, vol. 6, p. 2020, 2012.

[124] J. Björk, S. Stafström, and F. Hanke, "Zipping up: Cooperativity drives the synthesis of graphene nanoribbons," *J. Am. Chem. Soc.*, vol. 133, p. 14884, 2011.

[125] R. Gillen and J. Robertson, "Density functional theory screened-exchange approach for investigating electronical properties of graphene-related materials," *Phys. Rev. B*, vol. 82, p. 125406, 2010.

[126] E. Rudberg, P. Sałek, and Y. Luo, "Nonlocal exchange interaction removes half-metallicity in graphene nanoribbons," *Nano Lett.*, vol. 7, p. 2211, 2007.

[127] X. H. Qiu, G. V. Nazin, and W. Ho, "Vibronic states in single molecule electron transport," *Phys. Rev. Lett.*, vol. 92, p. 206102, 2004.

[128] A. Bérces, R. M. Dickson, L. Fan, H. Jacobsen, D. Swerhone, and T. Ziegler, "An implementation of the coupled perturbed Kohn-Sham equations: Perturbation due to nuclear displacements," *Comp. Phys. Comm.*, vol. 100, p. 247, 1997.

[129] J. Franck and E. G. Dymond, "Elementary processes of photochemical reactions," *Trans. Faraday Soc.*, vol. 21, p. 536, 1926.

[130] E. Condon, "A theory of intensity distribution in band systems," *Phys. Rev.*, vol. 28, p. 1182, 1926.

[131] N. S. .Wingreen, K. W. Jacobsen, and J. W. Wilkins, "Resonant tunneling with electron–phonon interaction: An exactly solvable model," *Phys. Rev. Lett.*, vol. 61, p. 1396, 1988.

[132] N. S. Wingreen, K. W. Jacobsen, and J. W. Wilkins, "Inelastic scattering in resonant tunneling," *Phys. Rev. B*, vol. 40, p. 11834, 1989.

[133] F. Guinea, A. H. Castro Neto, and N. M. R. Peres, "Electronic states and Landau levels in graphene stacks," *Phys. Rev B*, vol. 73, p. 245426, 2006.

[134] K. F. Mak, J. Shan, and T. F. Heinz, "Electronic structure of few-layer graphene: Experimental demonstration of strong dependence on stacking sequence," *Phys. Rev. Lett.*, vol. 104, p. 176404, 2010.

[135] J. Bardeen, L. N. Cooper, and J. R. Schrieffer, "Theory of superconductivity," *Phys. Rev.*, vol. 108, p. 1175, 1957.

[136] N. B. Kopnin, T. T. Heikkilä, and G. E. Volovik, "High-temperature surface superconductivity in topological flat-band systems," *Phys. Rev. B*, vol. 83, p. 220503, 2011.

Errata

In Eq. (9), $|n-1|$ should be substituted by $1-|n-1|$. The corrected version of the equation is

$$e_{\mathrm{xc}}(n,U) = \alpha_1(e^{-\alpha_2 U^2} - 1)e^{-(\alpha_3(1-|n-1|)-\alpha_4)^2}.$$ (4.1)

All calculations were done using the correct version of the equation, and the numerical results and conclusions remain unchanged.

BUSINESS +
ECONOMY

ART +
DESIGN +
ARCHITECTURE

SCIENCE +
TECHNOLOGY

CROSSOVER

DOCTORAL
DISSERTATIONS